Chinese Journal of Chemical Engineering 87 (2025) 204–219

Contents lists available at ScienceDirect

Chinese Journal of Chemical Engineering

journal homepage: www.elsevier.com/locate/CJChE

Full Length Article

Graphene oxide-polyethyleneimene-silicon dioxide nanocomposite-doped polysulfone ultrafiltration membrane oily water treatment

Hind Ben Youssef [1, 2], Ahmed T. Yasir [1, 2], Abdelbaki Benamor [1, 2, *]

[1] Gas Processing Centre, College of Engineering, Qatar University, 2713 Doha, Qatar
[2] Department of Chemical Engineering, College of Engineering, Qatar University, 2713 Doha, Qatar

ARTICLE INFO

Article history:
Received 9 January 2025
Received in revised form
10 March 2025
Accepted 6 May 2025
Available online 22 May 2025

Keywords:
Ultrafiltration membrane
Polysulfone
Graphene oxide
Silicon dioxide
Polyethyleneimine
Produced water

ABSTRACT

This study synthesizes and evaluates a novel polysulfone-based membrane doped with graphene oxide-polyethyleneimine-silicon oxide (GO-SiO_2-PEI), specifically designed for oily water treatment applications. The functionalization of graphene oxide with SiO_2 and PEI was rigorously confirmed through comprehensive XRD, FTIR, Raman spectroscopy, and XPS analyses, ensuring the integrity and expected functionality of the nanocomposite. This nanocomposite was integrated into the polysulfone (PSF) membrane matrix, significantly reducing the membrane's inherent hydrophobicity and propensity for fouling. The membranes were meticulously characterized using advanced surface and bulk sensitive apparatus including contact angle and SEM imaging to ascertain their structural and functional attributes. Performance evaluations conducted in a dead-end filtration setup revealed that incorporating 1.0% (mass) of the nanocomposite into the PSF membrane markedly enhanced its porosity and improved the water contact angle. This modification led to an 809% increase in the membrane's water flux and a 57% enhancement in flux recovery rate, while still maintaining a high oil rejection rate and a relatively low leaching rate of 5.3 $mg \cdot L^{-1}$. Analysis through the Owens-Wendt-Kaelble model indicated a significant increase in polar surface energy, corroborating the improved oil rejection capabilities at elevated flux levels. Fouling behavior, analyzed using Hermia's model, identified cake formation as the primary fouling mechanism in most of the tested membranes. Leaching tests further highlighted those membranes with higher nanocomposite loadings exhibited increased leaching rates, suggesting a trade-off between performance enhancement and material stability.

1. Introduction

Produced water (PW) is one of the prevalent waste streams in oil and gas production facilities. It represents a significant volume ratio of 3:1 for oil production and 4:1 for gas wells [1]. In 2021, Qatar Energy reported a substantial production of 77 million tons of liquified natural gas (LNG) and anticipated to increase its production capacity to a 142 million tons per annum by the year 2027 leading to the generation of significant volumes of PW, which emphasizes the urgent need for developing effective management and treatment approaches to handle the environmental and operational challenges associated with PW. PW contains impurities including heavy hydrocarbons, oils, heavy metals, and others [2]. These pollutants must be removed from water to meet the tolerable maximum oil discharge concentration of 40 $mg \cdot L^{-1}$ [3].

The current repertoire of PW treatments available are adsorption [4], biological treatments [5], coagulation [6], dissolved air flotation [7], and membrane filtration [8]. Each approach offers distinct properties in targeting specific contaminants and achieving the desired water quality standards. Membrane technology concedes as a leading technology for produced wastewater treatment for oil-in-water emulsions due to its numerous advantages. Firstly, membranes possess a specialized capability to separate water from specific impurities, achieved through the selective removal of undesirable molecules based on their molecular weight, surface charge, and size [9]. Moreover, membranes are considered to be non-hazardous due to the minimal use of chemicals and their ability to produce high water quality [10–12]. Additionally, membranes are considered to be relatively cost-effective, easy to operate, and achieves high rejection [13]. Membranes are categorized into two main types: polymeric and ceramic depending on their construction material [14,15]. Membrane filtration is categorized into 4 main types of filtrations which include ultrafiltration, microfiltration,

* Corresponding author.
E-mail address: benamor.abdelbaki@qu.edu.qa (A. Benamor).

https://doi.org/10.1016/j.cjche.2025.05.001

reverse osmosis, and forward osmosis. The selection of the appropriate type of filtration is based on the anticipated effluent water's quality and size of the targeted contaminant. Halleb *et al.* [16] highlighted that nanofiltration and ultrafiltration are effective for suspended particles enhancing its potential industrial use.

Nanocomposites have garnered significant attention in polymeric membranes due to their ability to enhance separation performance, hydrophilicity, and antifouling properties. Various nanomaterials, such as MXene, MOFs, PBAT, and MWCNTs, have been explored for this purpose, each offering distinct advantages, including improved water permeability, structural stability, and contaminant rejection [17–20]. Among these, graphene oxide (GO) stands out for its remarkable hydrophilicity, high surface area, and abundant oxygen-containing functional groups. These features promote better dispersion in polymer matrices and stronger interactions with polymer chains [21,22]. GO's nanoscale pores and interlayer spaces effectively restrict the flow of large oil droplets while allowing water molecules to pass through, mainly through size exclusion [23,24]. Moreover, the intrinsic hydrophilicity of GO, due to its high polarity, attracts polar water molecules while repelling non-polar oily molecules, resulting in enhanced water permeability and oil rejection [25,26]. GO also forms non-porous channels that offer high thermal and mechanical stability and can be easily dispersed in both organic and aqueous solutions [27]. Kuzminova *et al.* [28] synthesized polymeric membranes incorporating different compositions of GO-TiO_2 nanocomposites, achieving optimal anti-fouling performance with BSA rejection exceeding 98% and a flux recovery of 84%. However, fouling becomes more pronounced with increasing water flux, as organic matter rapidly accumulates on the membrane's surface, emphasizing the importance of functionalization [29]. These unique properties make GO an ideal nanocomposite for enhancing membrane performance in oily water treatment. Therefore, GO was selected as the primary additive in this study.

In literature, silicon dioxide (SiO_2) has demonstrated high performance in polymeric membranes for rejecting various impurities, including oils, dyes, heavy metals, and organic contaminants [30–32]. The incorporation of SiO_2 in polymeric membranes is expected to improve the membrane's oleophobic property ensuring effective separation of oil from water. The functional group ≡Si—O—Si≡ helps in the formation of membrane's micropores, improving its hydrophilicity and enhancing its antifouling tendency [33]. SiO_2 builds a layer on the membrane surface preventing deposition of oil particles which improves the membrane's fouling properties and its rejection [34]. Ebrahimi *et al.* [34] created a hydrophilic PAN/GO/SiO_2 electrospun membrane yielding a high permeance of 143 LMH·bar^{-1} ($L \cdot m^{-2} \cdot h^{-1} \cdot bar^{-1}$, 1 bar = 0.1 MPa), and a rejection of more than 98%. Using BSA as a foulant model, Liu *et al.* [35] demonstrated that GO-SiO_2 nanocomposite imbedded polyamide ultrafiltration membranes, had high anti-fouling performance compared to pristine membrane which resulted in a flux improvement by 24%. However, the membrane was tested only for salt rejection including NaCl, Na_2SO_4, $MgSO_4$ with no reported data for oil rejection.

Polyethylenimine (PEI) demonstrates effective performance as an additive in nanocomposites. PEI consists of highly positively charged functional amine groups that act on the repulsion of the negatively charged fouling organic matter. Its corporation evidenced substantial improvement in membrane's anti-fouling performance. Zhang *et al.* [36] developed GO-PEI nanocomposite incorporated into a polymeric membrane, achieving a retention factor of more than 97% and significant enhancement of relative flux recovery from 41.3% to 86.4% with increased composition of GO-PEI in the membrane. Parsamehr *et al.* [37] reported improved mechanical stability due to the crosslinking of GO with PEI through the crosslinking reactions between the carboxyl groups in GO and the amine charge of PEI resulting in improved filtration and selectivity. Matindi *et al.* [38] reported water flux enhancement of 41%, improved membrane hydrophilicity of 34%, and diminished fouling tendency by 50% in layered polyethersulfone (PES) UF membrane with a PEI-TiO_2 nanocomposite. Teng *et al.* [39] reported that their PEI/epoxied-SiO_2 coated PVDF membrane exhibited excellent antifouling resistance, where the best performing membrane achieved a very high flux recovery rate of 96.3% and a very low irreversible fouling ratio (DRir = 3.7%), confirming that the strong hydrated layer formed by the crosslinked coating effectively prevented BSA deposition. Moreover, Hussein Al-Timimi *et al.* [40] functionalized SiO_2 with PEI through covalent bonding between silanol groups and amine functionalities, potentially facilitated by silane coupling agents, along with additional electrostatic and hydrogen bonding interactions. Therefore, the use of PEI is particularly advantageous in pressure-driven membrane filtration.

Long term integrity and operability of membranes necessitates the development of effective cleaning technologies and exploring fouling-resistant membrane materials to preserve water resources and ensure their economic viability [41]. Analyzing membrane systems fouling *via* proven modeling tools is very important as it offers a comprehensive understanding of the complex interactions governing fouling phenomena and mechanisms [42]. Available models in the literature focus on characterizing the physical and chemical properties of membranes allowing a good understanding of their fouling dynamics using different approaches without specifying the underlying mechanisms [43]. Hermia [44] introduced four distinct models to address different fouling modes namely, pore constriction, complete blocking, intermediate blocking, and cake formation.

The objective of this work is to develop a novel ultrafiltration polysulfone (PSF) membrane incorporating super oleophobic (GO-PEI-SiO_2) nanocomposite. To the authors best knowledge, no significant literature on further functionalization of GO-SiO_2 with the polymer PEI to tackle the issue of fouling in produced water treatment is reported. This approach seeks to address the membrane fouling issues and oil removal efficiency in PW treatment by combining GO-SiO_2 unique properties with the antifouling properties of PEI and providing a promising solution for efficient membrane-based PW treatment compared to existing membrane technologies.

2. Experimental

2.1. Materials

Graphite powder (99.9% (mass)), potassium permanganate ($KMnO_4$, 99.9% (mass)), sodium nitrate ($NaNO_3$, 99.9% (mass)), hydrogen peroxide (H_2O_2, 30% (mass)), *N*-methyl-2-pyrrolidone (NMP, 99.9% (mass)), tetraethyl orthosilicate (TEOS, 99.9% (mass)), polyethylenimine (PEI, M_w 600), dimethylformaldehyde (CH_2O, 99.9% (mass)), (3-aminopropyl)triethoxysilane (APTES, 99.9% (mass)), and polysulfone pellets (M_w 35000, assay) were purchased from Sigma Aldrich. Ethanol absolute (C_2H_5OH, 99.9%% (mass)), was obtained from VWR Chemicals. Bovine serum albumin (BSA, 99.9% (mass)), with an average diameter of 7.4 nm was purchased from Fisher Scientific. The oil emulsion prepared for the rejection test consisted of 1000 mg·L^{-1} QALCO® performance oil, dispersed in distilled (DI) water using Ultra Turrax T25 (IKA) homogenizer following the procedure described erlier [45]. The oil properties are summarized in Table 1.

2.2. Synthesis of graphene oxide

The synthesis of GO, as outlined by Yasir *et al.* [46], follows the modified Hummers' method [47] used by Mahmoudi *et al.* [48].

Table 1
Oil properties used in the emulsion.

Flash point	220 °C
Appearance	Clear amber yellow
Physical state	Liquid
Vapor density (air = 1)	>1
Solubility in water	Negligible
Specific gravity	0.875
Viscosity	42–50 $mm^2 \cdot s^{-1}$
Conductivity	<0.001 $\mu S \cdot cm^{-1}$

Initially, 115 ml of H_2SO_4 was mixed with 5 g of graphite powder and 2.5 g of $NaNO_3$ in a 1000 ml beaker and stirred for 30 min in an ice bath while keeping the temperature below 20 °C to prevent overheating and explosion. Then, 15 g of $KMnO_4$ was carefully added to the mixture over a 2 h interval and the mixture's temperature was raised to 35 °C and maintained for 1 h at the same temperature. Progressively, 230 ml of deionized water was added to the mixture, causing a significant increase in temperature that should be maintained below 100 °C by controlling the rate of water dilution. The mixture was stirred for another 1 h, after which 300 ml of distilled water was added. To ensure the completion of the reaction, 10 ml of H_2O_2 was added to the mixture causing the mixture to exhibit a vibrant yellow colour signifying the reduction of all $KMnO_4$. The product was cleaned with HCl and water respectively before being filtered and freeze-dried, GO sheets were thus obtained.

2.3. Synthesis of GO-SiO_2-PEI

2.3.1. Synthesis of GO-SiO_2

The synthesized GO was functionalized with SiO_2, according to the procedure described by Dan *et al.* [49]. For this purpose, 125 ml alcohol-water solution was prepared by blending 25 ml of water and 100 ml of ethanol, followed by the addition of 0.6 ml TEOS. The mixture was maintained at a pH value of 4 using an acidic solution previously prepared by mixing 2 ml of acetic acid with 100 ml of water, added dropwise to the ethanol and TEOS mixture. In parallel, GO mixture solution was prepared by adding 0.125 g of GO to 150 ml of ethanol and maintained at a pH of 9 using an alkaline solution formulated by adding 2 ml of ammonia to 100 ml of water. The prepared alkaline aqueous solution was added dropwise to the GO-ethanol mixture until a pH of 9 was reached. Finally, the acidic and alkaline solutions were mixed and continuously stirred for 24 h. The GO-SiO_2 was extracted from the solution by vacuum cleaning multiple times to ensure maximum separation. Finally, the extracted nanoparticle was freeze-dried.

2.3.2. Synthesis of GO-SiO_2-PEI

Following the approach described by Wang and Ge [50], GO-SiO_2 was further functionalized with PEI. 0.0888 g of GO-SiO_2 was dispersed in 100 ml ethanol under continuous sonication to ensure its homogeneous dispersion, then, 4 ml of APTES was added to the sonicated mixture and kept at 50 °C under reflux for 24 h to allow completion of the reaction. The APTES-GO-SiO_2 nanoparticle was then extracted from the solution by vacuum cleaning followed by its dispersion in 100 ml of water under stirring. Subsequently, 0.5 ml of PEI was added dropwise to the mixture, to which another 6 ml of formaldehyde was added and left at 40 °C under reflux for 12 h. After completion of the functionalization process, GO-SiO_2-PEI nanoparticles were cleaned with ethanol and water respectively followed by freeze-drying. A brief schematic diagram of the synthesis procedure is illustrated in Fig. 1.

2.4. Fabrication of membranes

In this work, a total of six polysulfone-based membranes with different nanoparticle compositions were synthesized using phase inversion technique [51]. The synthesis process started with dissolving 6.14 g of polysulfone pellets in 25 ml NMP solvent. The mixture was maintained at 70 °C and continuously stirred at 300 $r \cdot min^{-1}$ using magnetic stirrer until complete dissolution of the PSF in the solvent. In parallel, 6.14 mg of the prepared nanoparticles were dissolved in 5 ml NMP solution and continuously sonicated for 30 min. Then, both prepared solutions containing polysulfone and nanoparticles were mixed together and left under gentle stirring for 48 h. Using a filmography doctor blade 360099003 (Braive Instrument, Germany), approximately 10 ml of the ultrasonicated solution was uniformly spread onto a glass plate. After that, the glass plate was dipped in deionized water bath where the film solidified, and the membrane was formed. Compositions of synthesized membranes are represented in Table 2.

2.5. Characterization of the nanoparticles

Synthesized nanoparticles were characterized using surface and bulk characterization techniques such as XPS, RAMAN, XRD and

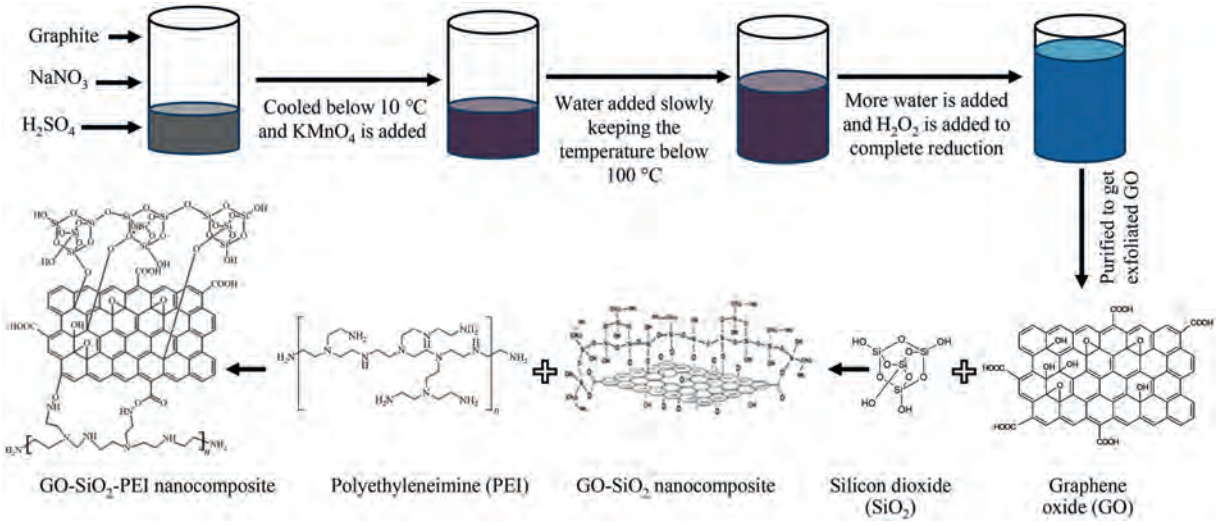

Fig. 1. Synthesis procedures of GO, GO-SiO_2, and GO-SiO_2-PEI nanocomposites.

Table 2
Compositions of the casting solutions.

	NMP/% (mass)	PSF/% (mass)	NP/% (mass)[①]	PSF: NMP: GPS
GPS-0.0	83	17	0.0	1:4.8:000
GPS-0.1	83	17	0.1	1:4.8:001
GPS-0.3	83	17	0.3	1:4.8:003
GPS-0.5	83	17	0.5	1:4.8:005
GPS-1.0	83	17	1.0	1:4.8:010
GPS-1.3	83	17	1.3	1:4.8:013

[①] Calculated based on the solid mass in the solution.

FTIR analyses. To identify the crystallinity of synthesized nanoparticles, XRD patterns were obtained using a PAN analytical X-ray diffractometer (Model: EMPYREAN), operated at 40 kV using a Cu Kα radiation ($\lambda = 0.15406$ nm) within a range of 5° to 90°. The FT-IR spectra were recorded using Thermo Scientific Nicolet iS10 in a wavelength range of 4000–500 cm^{-1} in transmittance mode at room temperature. To identifying the surface composition on the nanocomposite, X-ray photoelectron spectrometer model AXIS Ultra DLD, KRATOS XPS apparatus was used. To illustrate the structural changes of the GO and to confirm its functionalization with SiO_2 and PEI, RAMAN analysis was performed for the three nanoparticles using Thermo Fisher Scientific DXR Raman microscope with a wavelength of 532 nm, 40 times scanning, and the laser power used is 10 mW using 50× microscope objectives.

2.6. Characterization of fabricated membranes

2.6.1. Porosity and pore size tests

Using the gravimetric approach, the porosity of the membranes was characterized by weighing the same membrane sample at wet and dry conditions using an analytical balance having an uncertainty of 0.10%. The porosity (ε) was calculated using the following equation [24]:

$$\varepsilon = \frac{\omega_1 - \omega_2}{A \times l \times d_w} \tag{1}$$

In this case, ω_1 and ω_2 stand for the masses of wet and dry membranes in grams, respectively. l represents the membrane thickness in centimeters, d_w symbolizes the density of water, specifically 0.998 $g \cdot cm^{-3}$.

The membranes' pore radius was calculated using the Gueroult-Elford-Ferry equation as follows:

$$r_m = \sqrt{\frac{(2.9 - 1.75\varepsilon)8\eta l Q}{\varepsilon \times A \times \Delta P}} \tag{2}$$

where the variables η, Q, and ΔP stand for the viscosity of water (8.9×10^{-4} Pa·s), the volume of pure water permeated per unit time ($m^3 \cdot s^{-1}$), and the operating pressure (Pa).

2.6.2. Analysis of contact angle, cross-sectional morphology, and surface roughness

The morphology and surface roughness of the membranes were examined using atomic force microscopy (AFM). The surface roughness of the modified and pristine membranes were assessed using a multimode AFM with Nanoscope IIIa controller (Veeco, USA) and tapping mode with TESP cantilevers (Bruker AXS). The hydrophilicity of the membrane was examined using contact angle with the help of the DataPhysics contact angle analyzer (OCA15 Pro, Germany) by dropping DI water onto the membrane.

2.6.3. Oil rejection, flux, and fouling tests

Flux tests were conducted to examine the membranes' permeation using a dead-end cell (Sterlitech HP4750) maintaining the operating pressure at 6 bars supplied by compressed nitrogen. Membrane samples in circular shapes with areas of 14.6 cm^2 each were cut and placed inside the dead-end cell. Continuous stirring was provided in the dead-end cell to avoid concentration polarization. The permeate was collected in a beaker placed on a balance connected to a data acquisition system. Prior to any test, the membrane was compressed for 1 h before measuring the flux that was calculated using this equation [24]:

$$J = \frac{w_t - w_o}{A \times d_w \times \Delta t} \tag{3}$$

In this equation, w_o represents the initial mass of permeate water, while w_t represents the mass of permeate water at time t in grams. The letter A denotes the surface area of the membrane in square centimeters, d_w symbolizes the density of water and Δt denotes the duration of filtration in seconds.

Using protein BSA solution as a model foulant, the membranes' fouling tendency were tested using the same set up under similar conditions described earlier. The protein foulant solution was prepared by dissolving 1 g of BSA in 1 L of DI water. The procedure consists of measuring the DI water flux for 10 min according to Eq. (3) followed by measuring BSA solution flux for 90 min under the same operating conditions. Following the BSA fouling test, the membrane was cleaned with DI water, and a new record of DI water flux was taken for 10 min. Using the acquired fluxes data, the total fouling ratio (R_t), flux recovery ratio (FRR), reversible fouling ratio (R_r), and irreversible fouling ratio (R_{ir}) were calculated using the following equations:

$$R_t = \frac{J_{w0} - J_{wf}}{J_{w0}} \times 100\% \tag{4}$$

$$FRR = \frac{J_{w1}}{J_{w0}} \times 100\% \tag{5}$$

$$R_r = \frac{J_{w1} - J_{wf}}{J_{w0}} \times 100\% \tag{6}$$

$$R_{ir} = \frac{J_{w0} - J_{w1}}{J_{w0}} \times 100\% \tag{7}$$

where, J_{w0} represents the initial DI water flux, J_{wf} is the BSA permeate flux after 90 min, J_{w1} is DI water flux after cleaning.

2.6.4. Hermia's model: modeling of fouling mechanisms

The different fouling mechanism occurring on membrane surface was determined using Hermia's model, shown by the following mathematical equation [44]:

$$\left(\frac{d^2t}{dV^2}\right) = k\left(\frac{dt}{dV}\right)^n \tag{8}$$

where k is the resistance coefficient, and n is the characteristic model constant.

Depending on the fouling model determined, the value of n can be 0, 1, 1.5, and 2, representing cake layer formation, intermediate pore blocking, standard pore blocking, and complete pore blocking, respectively. The differential equation can be linearized in the following manner [44]:

$$n = 0, \quad \frac{1}{(J_{vt})^2} = \frac{1}{(J_{vo})^2} + \varepsilon_{cf} t \tag{9}$$

$$n = 1, \qquad \frac{1}{J_{vt}} = \frac{1}{J_{vo}} + \varepsilon_i t \tag{10}$$

$$n = 1.5, \qquad \frac{1}{\sqrt{J_{vt}}} = \frac{1}{\sqrt{J_{vo}}} + \varepsilon_s t \tag{11}$$

$$n = 2, \qquad \ln(J_{vt}) = \ln(J_{vo}) - \varepsilon_c t \tag{12}$$

2.7. Leaching study

Leaching tests were carried out to check the integrity of GO-SiO_2-PEI membranes by measuring the leached amounts of nanocomposites from the polymeric membrane. The methodology described by Zhang *et al.* [52] was followed. A membrane in a circular form having a cross-sectional area of 14.6 cm^2 was cut and immersed in 50 ml DI water in a sample tube. The sample tube was maintained for 7 days, and then it was tested for the presence of nanoparticles, whose concentration was identified by testing the total organic compounds in the water sample with the help of TOC analyzer.

3. Results and Discussion

3.1. Characterization and analysis of the nanocomposites

3.1.1. RAMAN spectra

To illustrate the structural changes of the GO and to confirm its functionalization with SiO_2 and PEI, RAMAN analysis was performed for the three nanoparticles as presented in Fig. 2. The presented GO spectrum exhibited the highest intensity situated at 1343 cm^{-1} and 1584 cm^{-1} which correspond to G and D bands respectively. The G band relates to the carbon atoms while D band is due to the structural irregularities on the GO sheets. These results are well aligned with those obtained by Liu *et al.* [53] and close to those obtained by Ning *et al.* [54] who reported GO and GO-SiO_2 characteristic peaks at 1337 cm^{-1} and 1595 cm^{-1} respectively. The functionalization of GO by SiO_2 resulted in the same peaks situated at 1340 cm^{-1} and 1585 cm^{-1} but at a depleted position as shown in Fig. 2. The functionalization of SiO_2 onto GO caused a decrease in the peak intensity in GO-SiO_2 compared to GO attributed to the decreased number of GO sheets in GO-SiO_2 [54]. Moreover, the ratio of 0.88 between the D and G bands I_D/I_G for GO decreased to a value of 0.99 in the case of GO-SiO. Further functionalization of GO-SiO_2 with PEI resulted in characteristic peaks positioned similarly to the previous spectra but at ominously lower intensities. The G band and D bands at GO-SiO_2-PEI spectra are positioned at 1325 cm^{-1} and 1603 cm^{-1}. In addition, the ratio between the D band and G band I_D/I_G in GO-SiO_2-PEI spectra increased compared to the ratio exhibited in the GO spectra, which is in accordance with the findings of Ziółkowski *et al.* [55]. The peak depletion is attributed to the disappearance and the reduction of the existing GO sheets.

3.1.2. XPS analysis

To examine the surface composition of the prepared nanocomposites, X-ray photoelectron spectrometer (XPS, model KRATOS-AXIS Ultra DLD) was used by conducting a surface elemental analysis of the nanocomposites which were examined for carbon, silicon, and oxygen elements. The GO spectra shown in Fig. 3 reveal intense peaks at binding energies of carbon (C 1s) at 283 eV and oxygen (O 1s) at 529 eV, which is coherent with the chemical composition of GO. Upon functionalization with SiO_2, additional peaks appear representing the element silicon (Si 2s) and (Si 2p) at binding peaks of 99 eV and 149 eV respectively as seen in the red curve. The peaks are not evident as the analysis shows the surface composition only. The results obtained in this work align with the findings given by Dong *et al.* [56], where the peaks lie at the same energy bindings with similar intensities. The polymer PEI has amine ($-NH_2$) functional groups, hence the further functionalization with PEI exhibited additional nitrogen (N 1s) peak as illustrated in the blue curve. In a study conducted by Xing *et al.* [57], the XPS spectra attained for GO-PEI@PAN membrane exhibited observable nitrogen, oxygen, and carbon peaks similar to those reported for GO-SiO_2-PEI, where both spectra had N 1s appeared at binding energy of 400 eV, confirming the compatibility with our findings.

3.1.3. XRD analysis

The synthesized nanoparticles GO, GO-SiO_2, and GO-SiO_2-PEI were analyzed using X-ray diffraction (XRD) apparatus for their morphology's analyses. The typical XRD pattern for GO is shown in Fig. 4, which shows a strong and crisp diffraction peak at 2θ = 10.28° with an interlayer distance of 0.86 nm signifying a high crystalline degree [58]. Li *et al.* [59] reported that the XRD spectrum characteristic peak of graphite was typically observed at ~25°, this

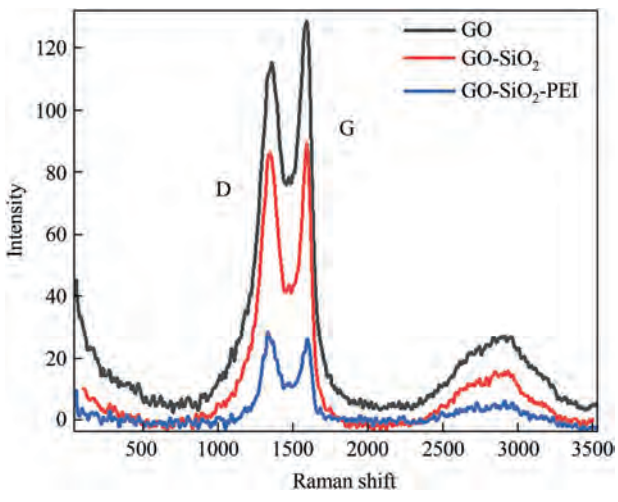

Fig. 2. RAMAN spectra of GO, GO-SiO_2 and GO-SiO_2-PEI.

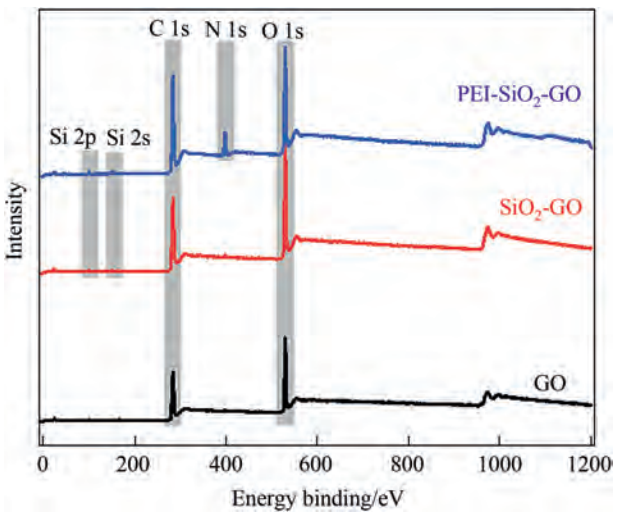

Fig. 3. XPS spectra for GO, GO-SiO, and GO-SiO_2-PEI.

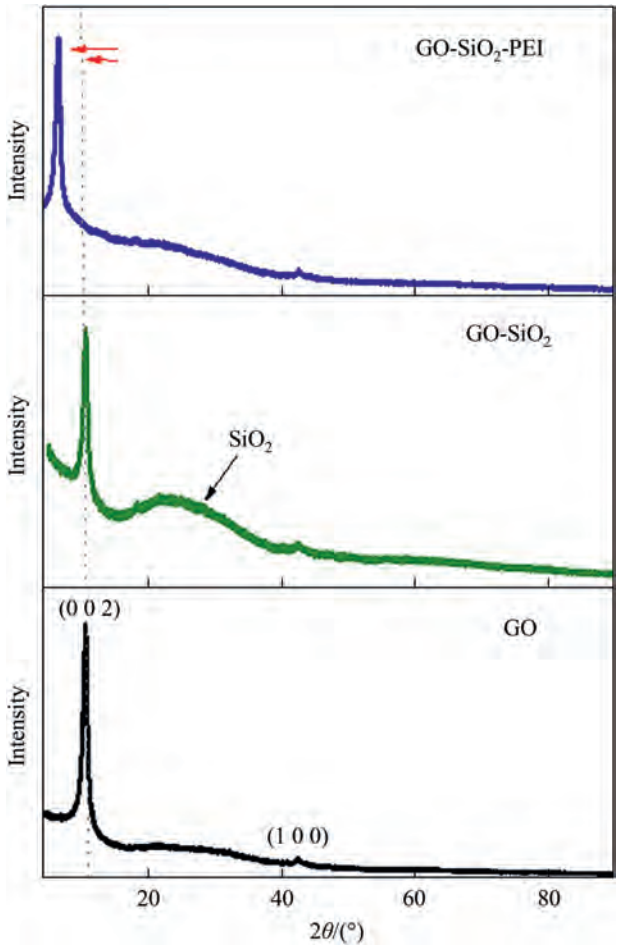

Fig. 4. XRD spectra for GO, GO-SiO_2 and GO-SiO_2-PEI.

decrease in the peak intensity can be attributed to the oxygen groups attached to the carbon. The functionalization of SiO_2 onto GO altered the GO peak and revealed a new peak attributed to the presence of SiO_2. The XRD spectra showed a shorter characteristic peak in the range of 10°–11° indicating a decrease in the crystallinity of the material which has become more amorphous as a result of GO functionalization with SiO_2. Moreover, a new broad peak observed in the range of 23°–25° attributed to the presence of SiO_2 which is in line with the XRD spectra reported by Kocyigit *et al.* [60]. Further addition of the functional groups of PEI causes a shift in the characteristic peak at a lower angle, where the peak lies between 5° and 7°. This is an indication that a functional group has been attached to GO leading to a decrease in crystallinity [61].

3.1.4. FTIR analysis

The FTIR spectra of GO, GO-SiO_2, and GO-SiO_2-PEI are presented in Fig. 5. The GO spectra exhibited multiple absorption bands at approximately 1220, 1640, 1710, and 3450 cm^{-1}, corresponding to the C—O atoms in carboxy and epoxy groups, the C=C atom in carboxyl groups, the C=O atom in carboxyl groups, and the stretching vibration of the —OH group, respectively. Furthermore, the fluctuations between 750 and 1050 cm^{-1} prove the presence of C=C with evident vibrational changes in the C=C bonds in the absorption bands spanning in the same range which agree with the results of the GO spectra reported by Surekha *et al.* [62]. Functionalization of GO with SiO_2 resulted in the appearance of more absorption peaks proving that the functionalization step was

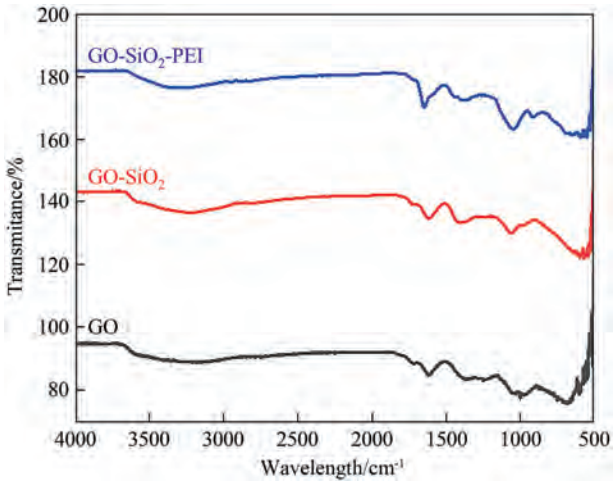

Fig. 5. FTIR spectra of synthesized nanoparticles.

successful. The bands allocated at 580 and 1058 cm^{-1} represent the stretching vibration of the O—Si—O, due to the asymmetric stretching vibrations of Si—O—C/Si—O—Si [63], while the band located at 971 cm^{-1} is due to the stretching vibrations of Si—OH as reported by Du *et al.* [64]. Finally, GO-SiO_2-PEI spectra showed additional bands in the range of 3200 to 3500 cm^{-1} with a peak located at 3392 cm^{-1} corresponding to stretching vibrations of NH_2 bond [53].

3.2. Characterization of membrane morphology and performance

3.2.1. Pore size, porosity, and contact angle test

The synthesized membranes were characterized by examining their pore sizes, porosity and their contact angles using SEM imaging. The pristine PSF membrane had a porosity of 51.38%, while the GO—SiO_2—PEI modified membranes exhibited higher porosity values ranging from 55.57% up to 73.99% depending on the nanoparticle loading as illustrated in Fig. 6. Silicon dioxide, used as nanofiller, has a high surface area-to-volume ratio and a strong interfacial contact between the nanoparticles and the surrounding polymer that causes the formation of larger pores [65]. The addition of nanoparticles to the membrane increased the membrane's porosity to a certain extent, however, beyond 1% concentration of the nanoparticles in the membrane a less significant impact on the porosity was observed. This increased concentration facilitated the movement of solvent out of the polymer matrix, resulting in the development of a more porous substructure and wider finger-like

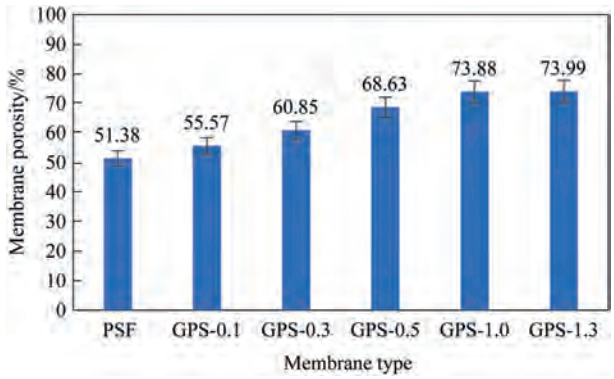

Fig. 6. Porosities for each membrane.

pores, resulting in membranes with higher nanocomposite loading exhibiting increased permeability. However, beyond 1.0% (mass) nanocomposite, excessive bulk led to nanoparticle agglomeration, causing slight pore blockage and a reduction in flux. This phenomenon has also been seen in a previous study by Yasir *et al.* [66].

The hydrophilicity of the membrane was examined by measuring its contact angle which indicates the membranes' affinity to water in a way that the membrane's contact angle decreases with increased membrane's affinity to water. The resulting contact angles for all membranes are shown in Fig. 7. With the addition of nanocomposite in the membrane's composition, the contact angle of the membrane decreased from 72° for pristine PSF to 63° for the membrane (GPS-0.1) containing 0.1% GO-SiO_2-PEI. A similar trend was observed for the remaining functionalized membranes. This is expected as the number of hydrophilic functional groups in the membrane increased and hence the hydrophilicity of the membrane increases.

The pore radius of the membrane was estimated and analyzed. The pristine PSF membrane's pore radius is estimated to be 6.09 nm as illustrated in Fig. 8. The incorporation of a minimum 0.1% nanocomposite in the membrane increased the pore radius to 7.69 nm. The trendline indicates that as the concentration of the GO-SiO_2-PEI increases, there is a corresponding enlargement in the pore radius until a maximum radius obtained with 0.5% nanocomposite, beyond which further addition of nanocomposite has no effect on the pore radius. The functional groups present in the nanocomposite such as the epoxy group (—O) in GO, the functional group (—Si—OH) in SiO_2, and the amino group in PEI all exhibit hydrophilic behavior towards the aqueous phase. Hence, during phase inversion, the nanocomposites migrate towards the aqueous phase from the organic phase creating hydrodynamic instability, resulting in formation of larger pores. Similar behavior has been observed in previous studies by Yasir *et al.* [66], Elhamarnah *et al.* [67], Alkhouzaam *et al.* [68].

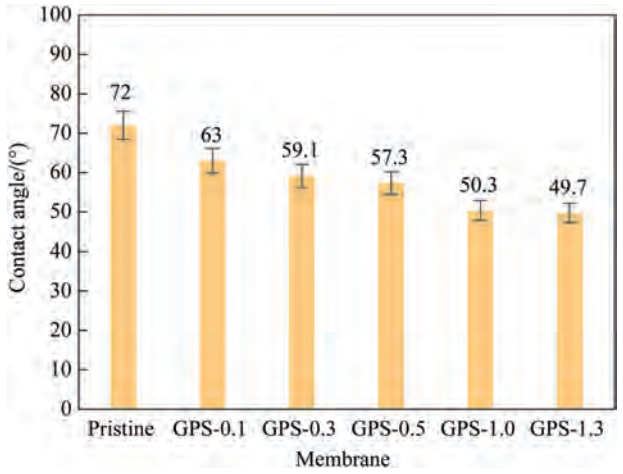

Fig. 7. Contact angles for each membrane.

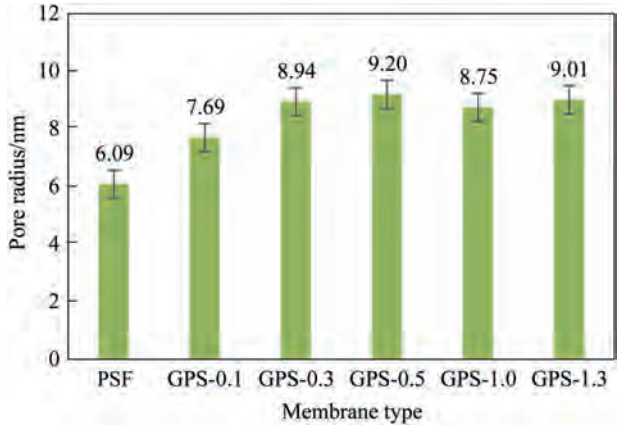

Fig. 8. Pore radius of synthesized membranes.

3.2.2. Surface morphological structure

The surface morphology of the membranes was investigated by obtaining SEM images using a scanning electron microscope (SEM; JSM-5610LV, JEOL, Tokyo, Japan). The membrane was submersed in ethanol for about 10 min and then immersed in nitrogen for 5–10 min with the help of tweezers. The dry rigid membrane was fractured into a smaller sample-sized piece. The sample was placed on a metal holder and different micrographs were taken. The SEM images of all membranes are shown in Fig. 9. The SEM images' top cross-sectional view shows a dense layer with tube-like pores in an unstructured manner that extends to the bottom layer. The hydrophilic functional groups in the nanocomposite GO-SiO_2-PEI such as the epoxy group (—O) in GO, (—Si—OH) in SiO_2, and the amino group in PEI migrate towards the aqueous layer from the organic layer during phase inversion, resulting in formation of larger pores. Consequently, the higher the concentration of the nanocomposite in the casting solution, the more functional groups are available which results in larger pores. Moreover, the SEM analysis also shows the thickness of the membrane to be between 75 and 90 μm. However, altering nanocomposite concentration did not affect the membrane thickness.

3.2.3. Surface membrane roughness

The membranes' surface roughness was examined using atomic force microscopy (AFM). It is a non-destructive characterization technique that is relatively new, which takes a high-resolution topographic image of the materials' surface such as nanoparticle or membranes with a scale of nanometer [69]. Fig. 10 represents the surface roughness of synthesized membranes while the corresponding numerical values are presented in Table 3.

The surface roughness of pristine PSF membrane is 7.42 nm while the RMS roughness is 9.92 nm. On the other hand, the membrane that is incorporated with 1.3% of the nanocomposite has an average roughness and RMS roughness of 7.73 nm and 10.27 nm respectively. The direct relationship between the amount of GO-SiO_2-PEI and the membrane roughness is logical since the more nanoparticles the membrane contains, the more functional groups available that disturb the surface resulting in surface fluctuations and variability. The trend of increase of the surface roughness parameters suggest that there's an increase in hydrophilicity as the nanocomposite percentage increases which in accordance with the Wenzel equation that related roughness to hydrophilicity [70]. However, as previously stated, the amount of hydrophilic functional groups plays a limiting factor hence the jump is not significant.

3.3. Membrane performance

3.3.1. Permeation flux of pure water

The obtained results for pure water flux of all synthesized membranes are summarized in Fig. 11. The polysulfone membrane resulted in a permeance of 5.54 LMH·bar^{-1} while the membrane that contained 0.1% of GO-SiO_2-PEI resulted in a permeance of 11.92 LMH·bar^{-1} which progressively increased as the amount of nanocomposite increased. This is attributed to the increase concentration of nanocomposite in the membrane that results in bigger pores

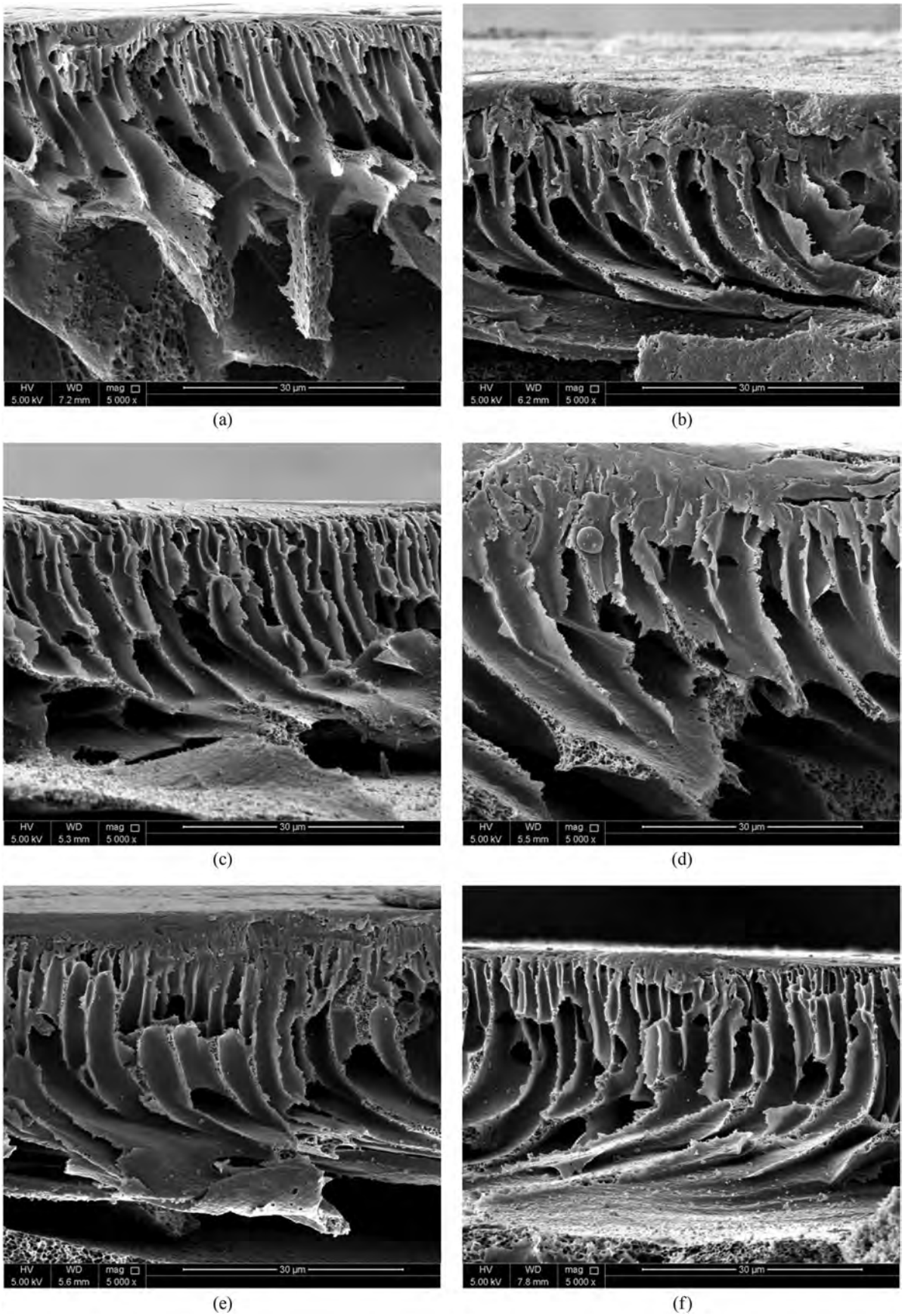

Fig. 9. Cross-sectional morphology of (a) unmodified membrane, (b) GPS-0.1, (c) GPS-0.3, (d) GPS-0.5, (e) GPS-1.0, (f) GPS-1.3.

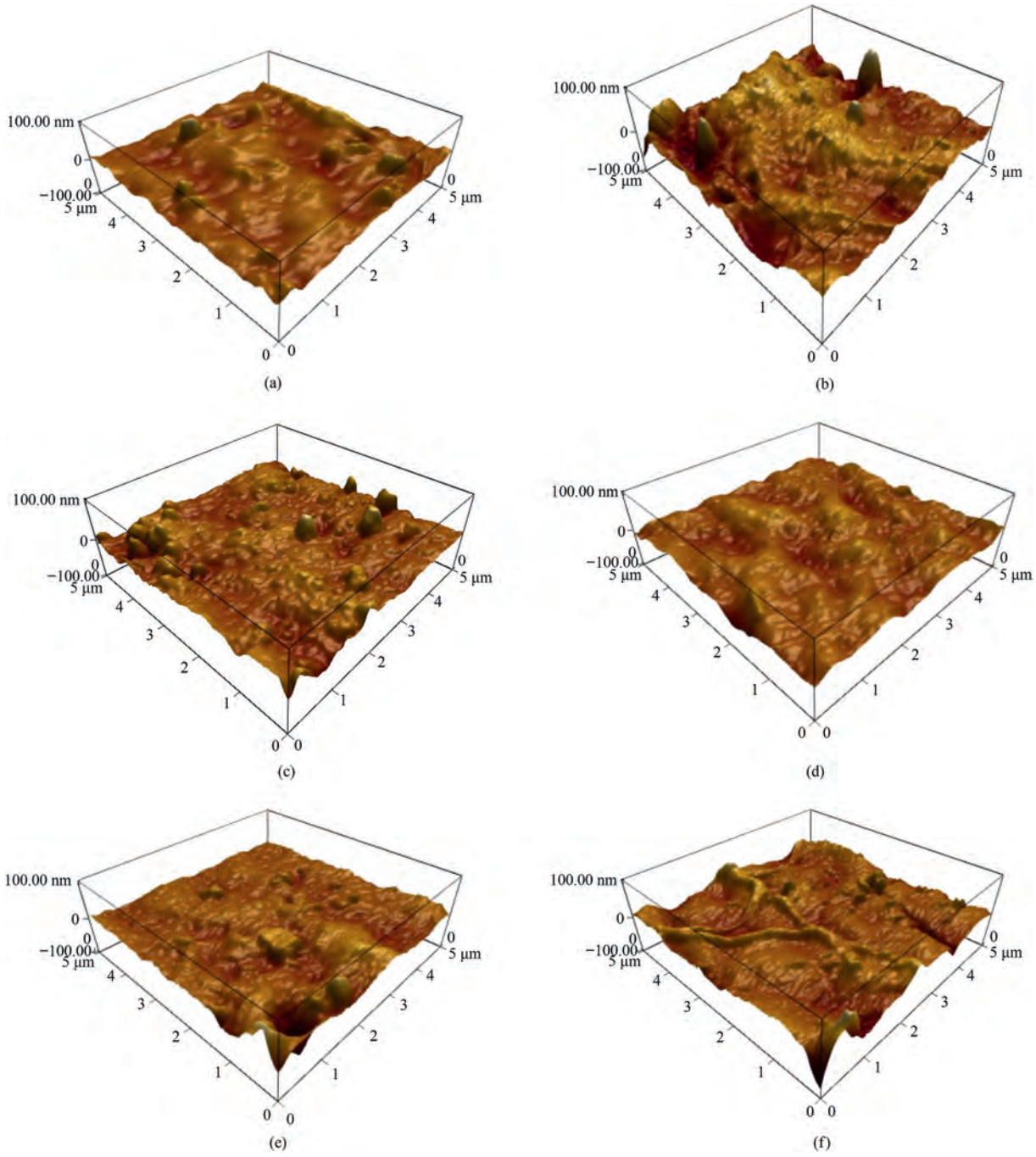

Fig. 10. Surface morphology of (a) PSF membrane, (b) GPS-0.1, (c) GPS-0.3, (d) GPS-0.5, (e) GPS-1.0, (f) GPS-1.3.

and higher porosity, hence more permeability as illustrated in Fig. 11. The maximum permeation flux achieved is 44.65 LMH·bar^{-1} for the membrane containing 1.0% nanocomposite before it decreases to 34.38 LMH·bar^{-1} for the membrane containing 1.3% nanocomposite. This behavior can be explained by the increasing concentration of nanoparticles, which clogs the pores more severely and obstructs the water flow.

A relation between membrane's porosity, contact angle and permeate flux is illustrated as a three-dimensional surface plot presented in Fig. 12. This figure provides a comprehensive visualization of how porosity and contact angle interact and influence simultaneously the membrane's flux. The surface demonstrates a clear relationship between the porosity, contact angle and the water flux. As the membrane's porosity increases and contact angle decreases, the membrane' water flux increases. This correlation is evident as the contact angle is an indication of the membrane's hydrophilicity whose decrease resulted in increased membrane's permeation flux. Furthermore, considering the membrane's porosity as the empty volume fraction of the membrane, its increase, prompts water permeation, hence leading to increased permeation flux.

3.3.2. Oil rejection test

The oil rejection tests were performed on the synthesized membranes using 1000 mg·L^{-1} of oil-water emulsion, and the results are summarized in Fig. 13. GPS-0.1 membrane has a rejection

Table 3
Membranes' roughness parameters.

Membranes	Average roughness/nm	RMS roughness/nm	Max/nm	Min/nm
PSF	7.42	9.92	55.19	−47.44
GPS-0.1	7.42	11.47	68.64	−65.49
GPS-0.3	7.42	9.66	48.42	−34.89
GPS-0.5	6.30	7.98	25.60	−0.90
GPS-1.0	6.49	9.36	69.49	−80.32
GPS-1.3	7.73	10.28	54.67	−64.51

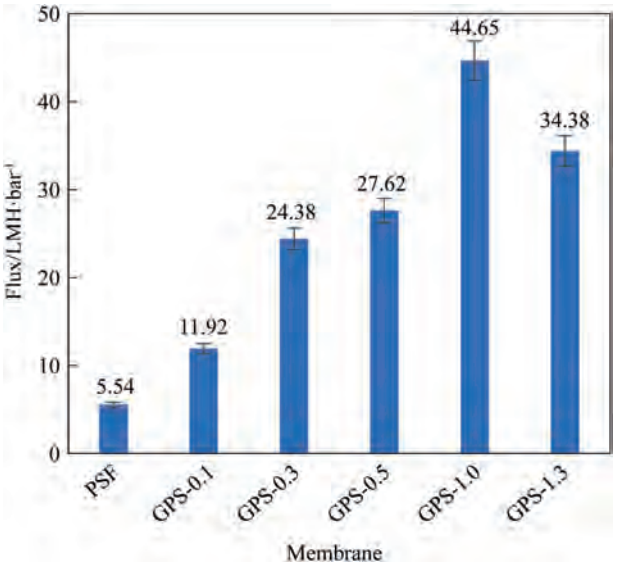

Fig. 11. Pure water fluxes of produced membranes.

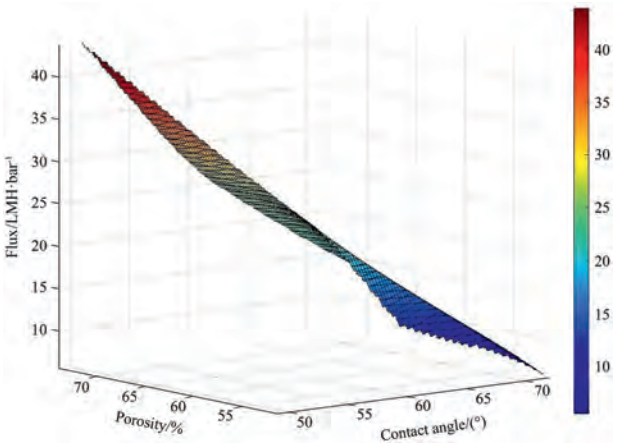

Fig. 12. 3D plot showing the relation between contact angle, porosity, and the flux.

percentage of 99.94% which decreased to 96.93% with increased percentage of incorporated nanocomposite to 0.3%. The increase of oil rejection is attributed to the increase amount of silicon in the membrane, which has an oleophobic property that repels the oil particles from the surface of the membrane [71]. Furthermore, the rejection remained consistent in a range between 99% and 97.64% with negligible fluctuations since the standard deviation is below 0.0, hence the oil rejection is considered to be independent on the amount of nanocomposite in the membrane. The hydrophilic and super oleophobic nanocomposite enhanced the water permeability and provided high oil rejection.

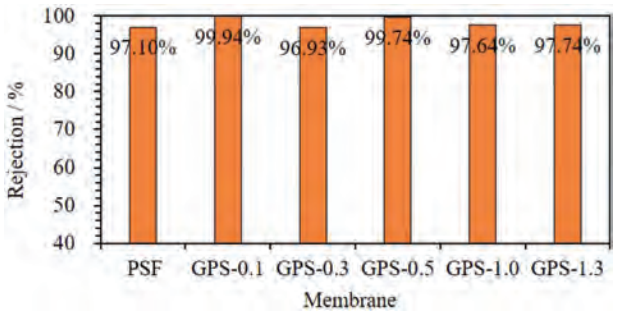

Fig. 13. Oil rejections for pristine polysulfone membrane and nanocomposite incorporated membranes.

A three-dimensional plot illustrating the effect of porosity and contact angle on the oil rejection is presented in Fig. 14. Here, rejection is represented along the *z*-axis, porosity along the *x*-axis, and contact angle along the *y*-axis. The membrane's contact angle is indirectly proportional to its rejection as the *ZY* plane displays. As the contact angle decreases, membrane's rejection increases until it reaches a steady value. This is evident as the membrane's hydrophilicity increases; it lowers the chances of oil droplets accumulating at the membrane surface. Moreover, in the *ZX* plane, the curvature illustrates an increase of rejection with the porosity increase until it reaches a steady value after which further changes in porosity have no significant effect on oil rejection. This trend can be explained by the increased amount of SiO_2 in the membrane matrix, which makes the membrane super oleophobic and repels the oil droplets from its surface, hence increasing the oil rejection.

The membrane's performance in oil rejection can be further elucidated through the concept of surface energy, which offers insights into the interactions between fouling particulates and surface membrane. Surface energy is categorized into dispersive (γ_s^d) and polar energy (γ_s^p) components which are estimated in accordance to Owens-Wendt-Kaelble (OWK) model. The estimated dispersive and polar energy components are visualized in Fig. 15. The pristine PSF membrane yielded a stronger γ_s^d compared to γ_s^p with values of 58 $mJ \cdot m^{-2}$, 23 $mJ \cdot m^{-2}$, respectively. This is due to the strong interactions between the non-polar droplets and surface membrane, which is consistent with the lower oil rejection performance as presented in Fig. 13. However, all nanocomposite incorporated membranes, γ_s^p is greater than γ_s^d. The estimated γ_s^p are 115 $mJ \cdot m^{-2}$, 146 $mJ \cdot m^{-2}$, 226 $mJ \cdot m^{-2}$, 191 $mJ \cdot m^{-2}$, 173 $mJ \cdot m^{-2}$ for GPS-0.1, GPS-0.3, GPS-0.5, GPS-1.0, GPS-1.3 respectively as illustrated in Fig. 15. This phenomenon can be attributed to the reduced polar interactions between the oil particles and membrane surface, leading to enhanced oil rejection performance as the

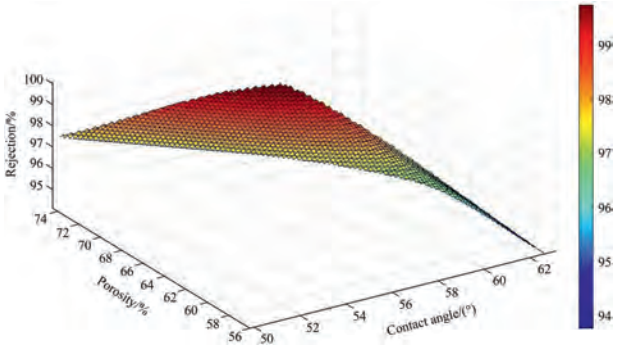

Fig. 14. 3D plot showing for contact angle, porosity, and rejection.

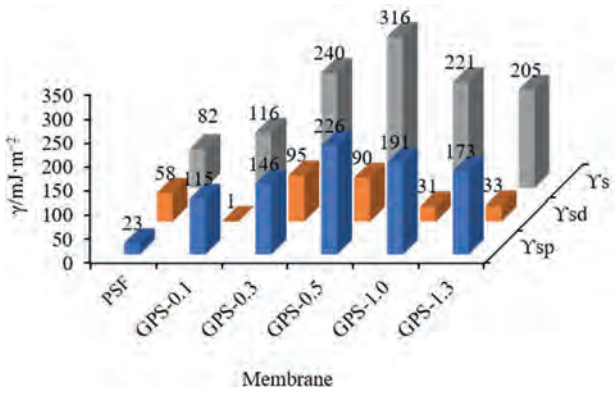

Fig. 15. Surface energies of produced membranes.

amount of nanocomposite increases. As shown in Fig. 13, incorporating nanocomposites into polymeric membranes resulted in consistently high oil rejection values, ranging from 97% to 99.9%. In addition, the dramatic difference between γ_s^p and γ_s^d is explained by the weak interaction between non-polar oil droplets and membrane surface.

3.3.3. Fouling test

The fouling test was carried out on the pristine and nanocomposite incorporated membranes using 1000 mg·L^{-1} of BSA in deionized water. The parameters that have been estimated for each membrane include total fouling, reversible fouling, irreversible fouling, and the flux recovery rate. The obtained experimental results are summarized in Fig. 16. The total fouling for pristine polysulfone membrane was estimated to be 88.9% which decreases to 61.6% for GPS-0.1 membrane before it increased again to 88.11% for GPS-0.3 and remained consistent with increased amount of nanocomposite in the membranes.

Fouling is impacted by the membrane characteristics such as pore size distribution, surface charge, hydrophilicity, and roughness. The distribution of bigger pore sizes affects easily the foulants to stick onto the membrane surface, which correspondingly affects the fouling tendency. Membranes with large pores can result in more noticeable membrane blockage as they offer higher opportunity for particle accumulation and pore blockage [72]. In addition, bigger pores have a greater blocking index than smaller ones under the same filtration operation conditions. This aligns with the results of this work, the pore size increases with the increase of the composition of the nanocomposite in the membrane as seen in Fig. 8, which correspondingly increased the total fouling as illustrated in Fig. 16.

Furthermore, as the composition of the nanocomposite in membrane increases, the more hydrophilic the membrane surface is due to the increased number of hydrophilic functional groups as explained earlier. The hydrophilicity of the membrane resists fouling tendency by enhancing foulant hydration, which reduces the adhesion of the particulates onto the membrane surface [72]. In addition, the hydrophilic functional group on the membrane has high water affinity which results in a water barrier on the surface preventing and limiting foulant accumulation. This was confirmed in this work, as the composition of GO-SiO_2-PEI increased, the irreversible fouling decreased while the reversible fouling increased as illustrated in Fig. 16. The flux recovery rate increased with increased nanocomposite composition in the membrane. The flux recovery rate estimated to be 17% for pristine polysulfone membrane, and surged to 58% for GPS-0.1. On the other hand, the irreversible fouling of the pristine polysulfone membrane that was 83% decreased significantly to 42% for GPS-0.1 and continued to decrease with increased nanocomposite loading.

Surface roughness influences the contact area between foulants and the membrane, which has a significant impact on the membrane fouling. The differences in contact areas, caused by the surface roughness, can have a major influence on the membrane fouling behavior. The texture on the membrane surface causes the foulants to get trapped on the surface and enhance the fouling. In this work, the surface roughness of the membranes remained consistent with the increase of the nanocomposite as seen in Table 3. Hence the addition of the nanocomposite did not have effect on surface roughness and hence it did not cause any additional fouling as illustrated in the total fouling rate which remained consistent in Fig. 16.

3.3.4. Determination of fouling mechanisms

The various fouling mechanisms occurring on each membrane surface were evaluated using Hermia's model. The flux rate using the BSA solution was calculated and used to plot several graphs as illustrated in Fig. 17 including (a) $1/(J)^2$ *vs.* time, (b) $1/J$ *vs.* time, (c) $\ln(J)$ *vs.* time and (d) $1/\sqrt{J}$ *vs.* time, corresponding to cake formation, intermediate pore blocking, complete pore blocking, and standard pore blocking, respectively. Additionally, the chi-squared value is calculated for each plot evaluating the fit of each fouling mechanism for the developed membranes, as presented in Table 4. The highest achieved R^2 for GPS-0.1 membrane was obtained from

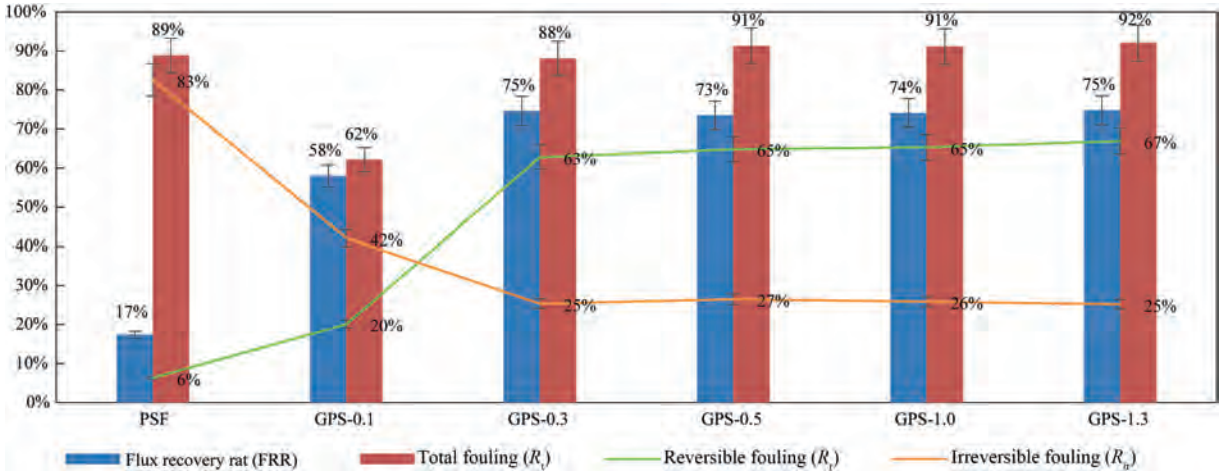

Fig. 16. Estimated fouling parameters for each membrane.

the pore blockage plot, indicating that complete pore blockage is the dominant fouling mechanism as the fouling particulates directly blocks the pores on surface membrane while delaying cake formation. In contrast, for all the other nanocomposite-incorporated membranes, the highest R^2 values were observed in the cake formation plot indicating that the fouling BSA material formed a thick cake layer on the membrane surface leading to significantly reduced water flux rate as well as greatly increasing the fouling tendency. These results confirm the fouling analysis findings: the GPS-0.1 membrane exhibited the lowest total fouling at 62%, while the other membranes experienced total fouling exceeding 88%. The PSF membrane, with its smaller pore radius, facilitated complete pore blockage and made cake formation the dominant fouling mechanism. In contrast, the GPS-0.1 membrane, with a larger pore radius than the PSF, allowed some BSA particles to pass through the pores, thereby delaying cake formation. Meanwhile, the GO-PEI-SiO_2 nanocomposite imparts a positive surface charge to the membrane. Increased nanocomposite concentration enhanced the attraction between BSA and the membrane surface, promoting foulant agglomeration and making cake formation the dominant fouling mechanism. Table 5 presents the fouling coefficient values that indicate the increase in fouling rate.

Analysis of the different fouling mechanisms obtained by plotting the GPS-0.1 membrane flux versus time as acquired by Hermia's model, we observe a non-linear curve that can be assimilitaed to the intersection of two distinct consecutive straight lines suggesting the presence of two distinct fouling mechanisms occurring sequentially. The first characteristic linear trendline, from zero to 55 min, indicates that pore blocking is the dominant fouling mechanism during the early phase of filtration given the chi-squared value reported in Fig. 18. Beyond 55 min, the second characteristic trendline illustrates a steeper slope, indicating a transition from pore blockage to the formation of a cake layer. This happens as the pores become fully blocked by BSA particulates and can no longer retain additional particles which accumulate on the membrane surface, leading to the formation of a cake layer. This two-phase fouling behavior suggests that the GPS-0.1 membrane is initially prone to pore blockage but eventually transits to cake formation as the fouling progresses. This phenomenon did not occur with membranes doped with higher nanocomposite concentration due to the stronger surface interactions (increased γ_s^p as seen in Fig. 15). The same behavior was observed in the remaining fouling mechanism plots, where each mechanism transitions into the cake formation phase, as shown in Fig. 18(b), (c), (d).

Table 4
Chi-squared values for each fouling mechanism for each membrane type.

	PSF	GPS-0.1	GPS-0.3	GPS-0.5	GPS-1.0	GPS-1.3
Cake	0.991①	0.723	0.984①	0.946①	0.988①	0.982①
Intermediate	0.976	0.767	0.947	0.909	0.988	0.930
Pore	0.933	0.802①	0.882	0.827	0.954	0.867
Standard	0.952	0.785	0.919	0.874	0.976	0.919

① Maximum chi-squared value indicating the dominant fouling mechanism.

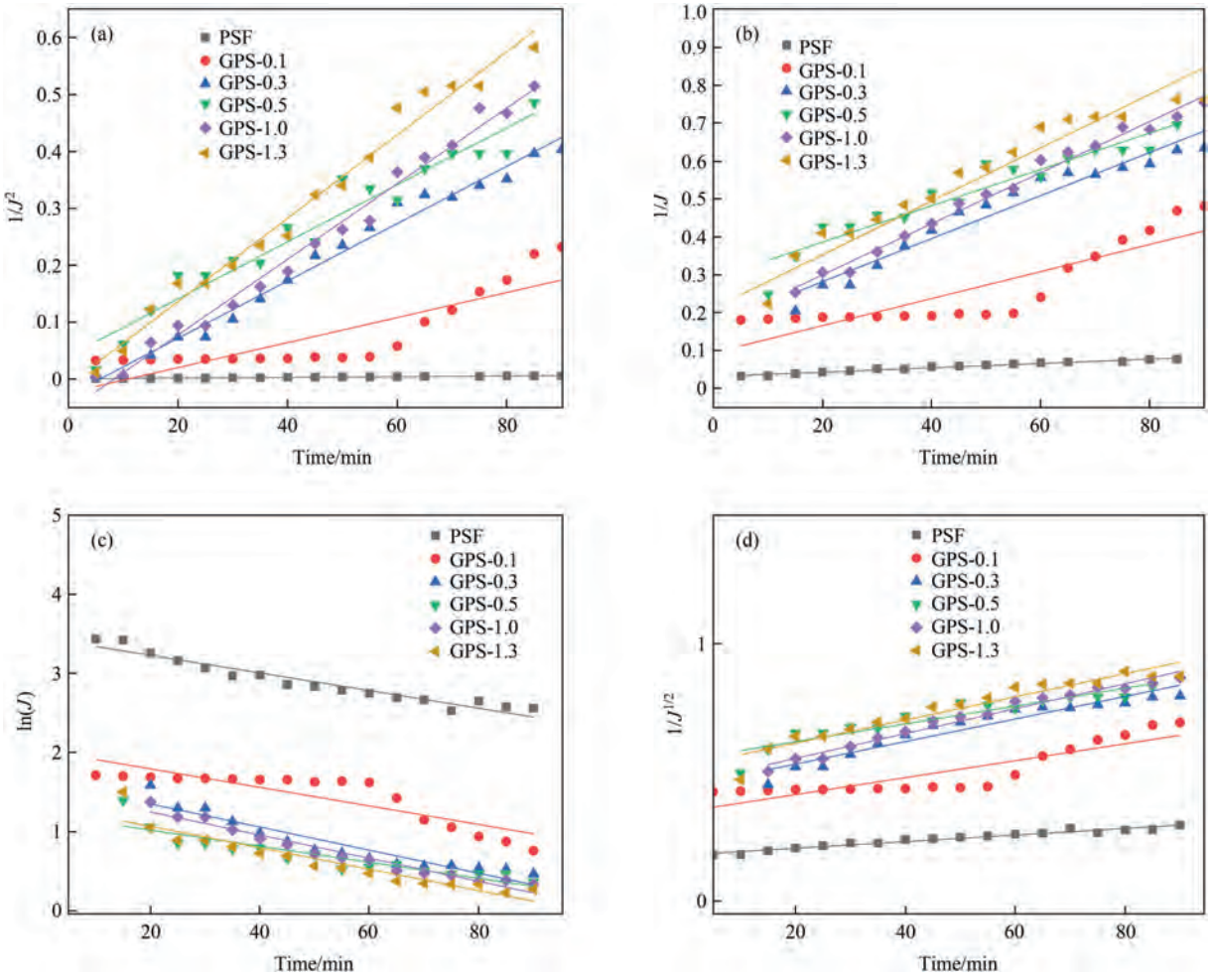

Fig. 17. Prediction of fouling mechanism using Hermia's model: (a) cake filtration, (b) intermediate pore blockage, (c) pore blockage, (d) standard pore blockage.

Table 5
Fouling coefficients for each membrane.

Membrane	Fouling coefficient
PSF	0.00006
GPS-0.1	0.00220
GPS-0.3	0.00504
GPS-0.5	0.00501
GPS-1.0	0.00664
GPS-1.3	0.00731

3.3.5. *Leaching test*

As explained in 2.7, leaching tests were performed for one week using all produced membranes to investigate the stability of GO-SiO_2-PEI nanoparticles in the membrane matrix. The leaching solution was examined for total organic carbon using TOC analyzer. The final TOC concentrations are summarized in Fig. 19. The GPS-0.1 membrane exhibited a relatively low organic carbon concentration of 1.014 mg·L^{-1}, indicating minimal leaching. The concentration of leached nanoparticle continued to increase with the highest concentration obtained for GPS-1.3 membrane estimated at 6.488 mg·L^{-1}, which signifies substantial leaching. The increased leaching tendency with increased nanocomposite loading can be related to the higher number of hydrophilic functional groups that have a strong attraction to water casing them to leach away from the membrane.

4. Comparative Analysis: GO-SiO_2-PEI Incorporated Membranes versus Other GO-Based Membranes

The parameters of the optimally synthesized membrane using the novel nanocomposite GO-SiO_2-PEI were analyzed. It was concluded that employing 1.0% of the nanocomposite resulted in one of the highest performances observed, with an impressive flux enhancement of 806% compared to the pristine PSF membrane.

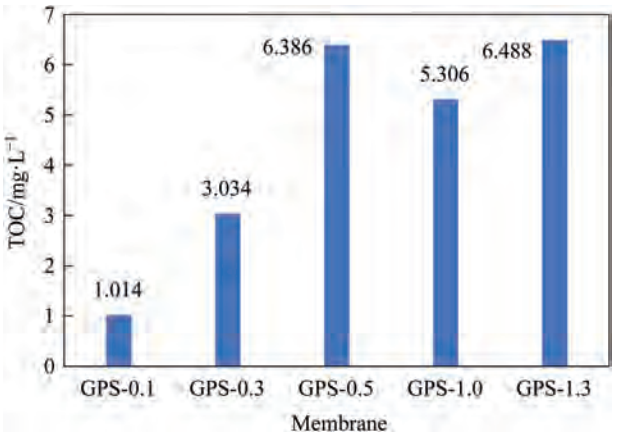

Fig. 19. Amount of leached nanoparticles for each membrane.

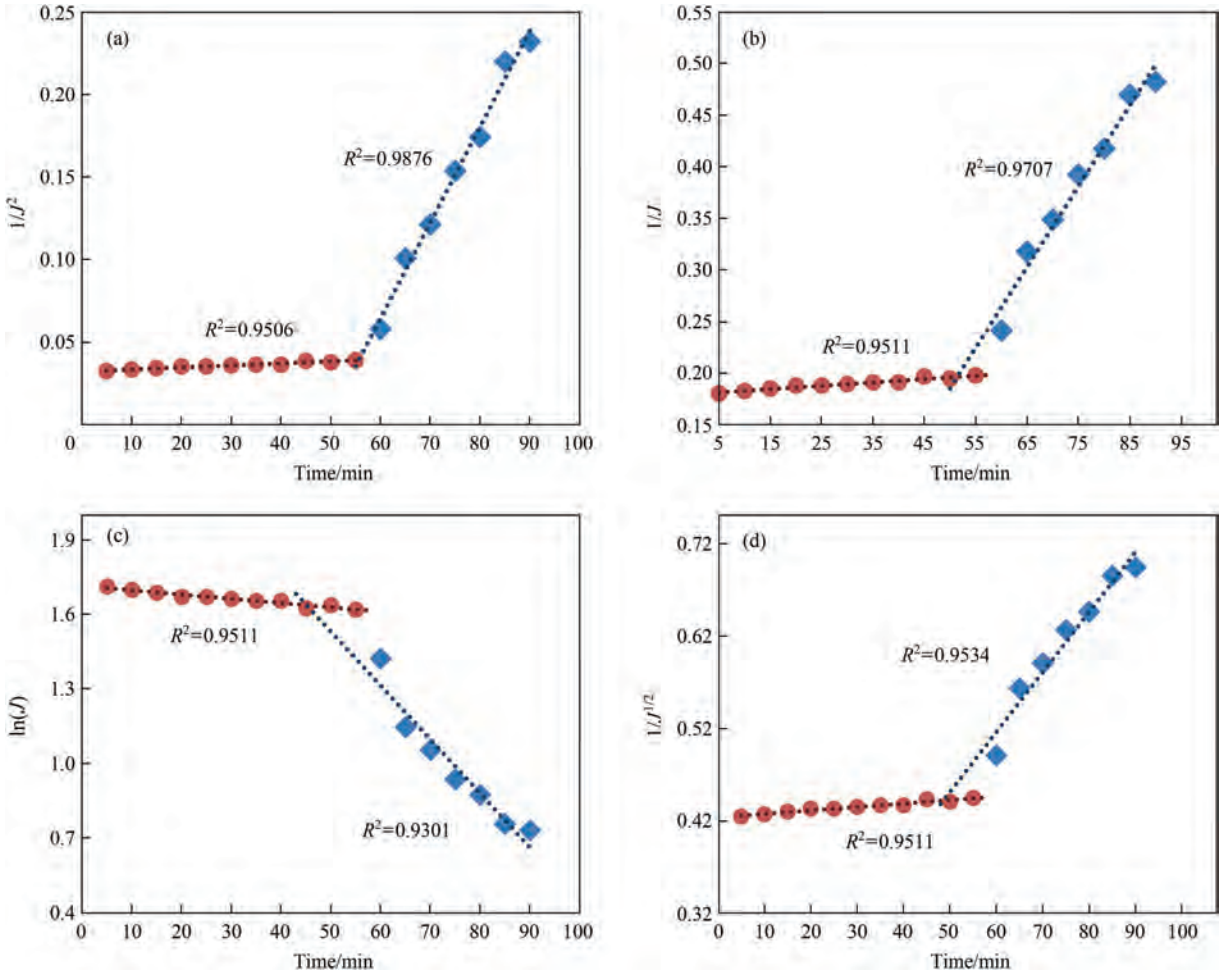

Fig. 18. Hermia's model for GPS-0.1 membranes at two different time durations: (a) cake filtration, (b) intermediate pore blockage, (c) pore blockage, (d) standard pore blockage.

Table 6
Comparative evaluation of GO-based membranes for enhancement in pure water flux, and oil-in-water separation.

Nanocomposite	Permeation flux enhancement compared to pristine membrane/%	Rejection/%	Anti-fouling performance	Contaminant	Reference
GO-PEI/PVP	164	>90	Flux decline: Reduced the flux to 80% efficiency.	BSA	[36]
PVDF-g-PMMA/GO@SiO_2	178	95	The permeance reduced by maximum of 0.2 LMH·bar^{-1}.	Soybean oil (266)	[33]
ZIF-8/rGO	~22	95	The flux recovery maintained high after 10 cycles.	Oil	[74]
A-SEP@TiO_2/GO	125	>99.7	The membrane retrieves the flux permeation after repeated fouling cycles.	*n*-Hexane	[75]
GO-PA-Fe^{3+}/PVDF	643	>99.5	The membranes flux decreased by 8.6% after 10 cycles with permeance range 38.2–41.8 LMH·bar^{-1} with rejection above 99%.	Palm cooking	[73]
SA/GO/CS	34	99.84	The flux recovery decreased by 9% for CS/GO while SA/GO recovery rate increased by 1.63% after 5 uses.	Soybean oil	[76]
GO-SiO_2-PEI	806	>97	Flux recovery rate is 74%, the irreversible fouling rate is 26% and the reversible fouling rate is 65%.	Oil	This work

Additionally, the membrane achieved a flux recovery rate of 74% and an oil rejection rate exceeding 97%. Moreover, the membrane exhibited satisfactory anti-fouling performance, with an irreversible fouling rate of 26% and reversible rate of 65%. The flux was easily recovered by rinsing the membrane with DI water. This work's findings are benchmarked against other GO incorporated membranes as summarized in Table 6. The studies shown in Table 6 indicated that most of the GO based nanocomposite membranes had a flux enhancement between 22% and 178%. However, the flux enhancement obtained by incorporating GO-PA-Fe^{3+}/PVDF was 643% [73]. This membrane also exhibited 99.5% palm oil rejection efficiency. However, a critical analysis is lacking that gives a comprehensive study on the fouling performance of the membrane using a standard membrane foulant. The study by Zhang *et al.* [36] used BSA as model foulant for their GO-PEI/PVP incorporated membrane. Incorporation of GO-PEI/PVP resulted in a flux recovery rate of 80%. However, in this study, the flux enhancement was only 164% and the study lacked oil rejection tests. Membranes from Gu *et al.* [74] doped with ZIF-8/rGO nanocomposite showed an oil rejection efficiency of 95% and the flux recovery rate was also observed to be consistent after 10 regeneration cycles. However, the flux enhancement achieved by ZIF-8/GO incorporated membrane was only 22% [33]. In contrast, another study reported in the table, a A-SEP@TiO_2/GO membrane achieved optimal oil rejection of 99.7%, however, its flux enhancement of 125% only, which falls short of desired performance. Again, the membrane fouling performance was not examined using a model foulant, it merely stated that flux was recovered after multiple fouling cycles. Considering all these factors, the membrane developed in this study by doping PSF with 1.0% GO-SiO_2-PEI nanocomposite is found to be more suitable for oil treatment processes.

5. Conclusions

In this study, a novel hydrophilic-superoleophobic GO-SiO_2-PEI nanocomposite was synthesized and incorporated into PSF membranes for the treatment of oily wastewater. The functionalization of GO with SiO_2 and PEI was confirmed through XRD, FTIR, XPS, and RAMAN spectroscopy, demonstrating successful surface modification. The optimized membrane (GPS-1.0) exhibited a 43.8% increase in porosity (from 51.38% to 73.88%), a 30.1% reduction in contact angle (from 72° to 50.3°), an 809% enhancement in pure water flux (from 5.54 LMH·bar^{-1} to 44.65 LMH·bar^{-1}), and a 57% improvement in flux recovery rate (from 17% to 74%), while maintaining a high oil rejection of 97.6% and exhibiting low nanocomposite leaching of 5.3 mg·L^{-1}, ensuring structural stability. The fouling resistance of the membrane significantly improved, with the irreversible fouling rate decreasing from 83% for pristine PSF to 26% for GPS-1.0, while the reversible fouling rate increased to 65%, facilitating easier regeneration. Hermia's model analysis revealed that the dominant fouling mechanism transitioned from complete pore blocking in the pristine PSF membrane to cake layer formation in the nanocomposite-incorporated membranes, confirming improved fouling resistance. Furthermore, surface energy analysis using the Owens-Wendt-Kaelble model demonstrated that the incorporation of GO-SiO_2-PEI increased the membrane's total surface energy, mainly due to an enhancement in its polar component, further contributing to the improved hydrophilicity and antifouling properties. These findings highlight the potential of GO-SiO_2-PEI-doped PSF membranes as an effective solution for treating produced water and oily wastewater. Future studies should focus on evaluating the membrane's long-term stability under real-world conditions and optimizing its regeneration potential over multiple operational cycles.

CRediT Authorship Contribution Statement

Hind Ben Youssef: Writing – original draft, Investigation, Formal analysis, Data curation. Ahmed T. Yasir: Validation, Resources, Methodology, Formal analysis, Conceptualization. Abdelbaki Benamor: Writing – review & editing, Supervision, Project administration, Funding acquisition.

Declaration of Competing Interest

The authors declare that they have no known competing financial interests or personal relationships that could have appeared to influence the work reported in this paper.

Acknowledgement

This research is made possible by Qatar University internal grant (i-GA-379) and graduate sponsorship research award (GSRA7-1-0510-20046) from Qatar National Research Fund (QNRF). SEM and RAMAN analyses were accomplished in the Central Laboratories unit (CLU), Qatar University. Open Access funding provided by the Qatar National Library.

References

[1] A. Echchelh, T. Hess, R. Sakrabani, Reusing oil and gas produced water for irrigation of food crops in drylands, *Agric. Water Manag.* 206 (2018) 124–134.
[2] J. Beyer, A. Goksøyr, D.Ø. Hjermann, J. Klungsøyr, Environmental effects of offshore produced water discharges: a review focused on the Norwegian continental shelf, *Mar. Environ. Res.* 162 (2020) 105155.

[3] H.D. Dawoud, H. Saleem, N.A. Alnuaimi, S.J. Zaidi, Characterization and treatment technologies applied for produced water in Qatar, *Water* 13 (24) (2021) 3573.
[4] R.C. Ye, H.S. Li, J.Y. Long, Y.X. Wang, D. Peng, Bio-aerogels derived from corn stalk and Premna Microphylla leaves as eco-friendly sorbents for oily water treatment: the role of microstructure in adsorption performance, *J. Clean. Prod.* 403 (2023) 136720.
[5] X.J. Zhang, J.P. Cheng, X. Liu, S. Yue, X.F. Wang, Y.F. Shi, N. Qiao, Computer assisted design and flow field analysis of a multi-tube airlift reactor for biological treatment of oily wastewater, *J. Water Process Eng.* 56 (2023) 104411.
[6] L.M. Wu, Y.X. Gao, X.F. Xu, J.J. Deng, H.S. Liu, Excellent coagulation performance of polysilicate aluminum ferric for treating oily wastewater from Daqing gasfield: responses to polymer properties and coagulation mechanism, *J. Environ. Manag.* 356 (2024) 120642.
[7] A. Scharnberg, H. Oliveira, S. Weschenfelder, J. Rubio, A. Azevedo, Flocculation of emulsified oil-in-water with dodecylbenzene sulfonate and polyacrylamide and floc separation by dissolved air flotation, *Colloids Surf. A Physicochem. Eng. Aspects* 669 (2023) 131496.
[8] M. Keyvan Hosseini, L. Liu, P. Keyvan Hosseini, K. Lee, J.H. Miao, Performance evaluation of a pilot-scale membrane filtration system for oily wastewater treatment: CFD modeling and scale-up design, *J. Water Process Eng.* 52 (2023) 103570.
[9] S. Karki, G. Hazarika, D. Yadav, P.G. Ingole, Polymeric membranes for industrial applications: recent progress, challenges and perspectives, *Desalination (Amst.)* 573 (2024) 117200.
[10] M. Padaki, R. Surya Murali, M.S. Abdullah, N. Misdan, A. Moslehyani, M.A. Kassim, N. Hilal, A.F. Ismail, Membrane technology enhancement in oil–water separation. A review, *Desalination (Amst.)* 357 (2015) 197–207.
[11] A.T. Yasir, N. Abounahia, M.Ali H. Saad, A. Benamor, An overview of membrane based NO_x removal technologies and denitrification filters, *Process Saf. Environ. Prot.* 197 (2025) 106951.
[12] M. Al-Ejji, D. Ponnamma, K. Zadeh, M. Zubair, A. Yasir, M. Hassan, N. Abdelhadi, K.N. Song, A.H. Hawari, Advanced membrane technology to remove boron from water and wastewater: a comprehensive study, *ACS Appl. Polym. Mater.* 5 (10) (2023) 7675–7697.
[13] A.Q. Al-Gamal, T.A. Saleh, Design and manufacturing of a novel thin-film composite membrane based on polyamidoamine-grafted graphene nanosheets for water treatment, *J. Water Process Eng.* 47 (2022) 102770.
[14] M.L. Chen, S.G.J. Heijman, L.C. Rietveld, Ceramic membrane filtration for oily wastewater treatment: basics, membrane fouling and fouling control, *Desalination (Amst.)* 583 (2024) 117727.
[15] L. Sawunyama, T.O. Ajiboye, O. Oyewo, D.C. Onwudiwe, Ceramic-polymer composite membranes: synthesis methods and environmental applications, *Ceram. Int.* 50 (3) (2024) 5067–5079.
[16] A. Halleb, F. Yokoyama, M.A. das Neves, M. Nakajima, Effects of surfactants and oil-in-water emulsions on reverse osmosis membrane performance, *Euro Mediterr. J. Environ. Integr.* 6 (2) (2021) 44.
[17] M. Ghadhban, K. Rashid, A. Abdulrazak, H. Meskher, Y. Benguerba, E. Yousif Al-Sarraj, Q. Alsalhy, Optimal operational conditions of PLA/PBAT mixed matrix membrane for the treatment of oily wastewater, *Eng. Technol. J.* 42 (9) (2024) 1179–1192.
[18] R. Imsong, D. Dhar Purkayastha, Dual-functional superhydrophilic/underwater superoleophobic 2D Ti_3C_2TX MXene-PAN membrane for efficient oil-water separation and adsorption of organic dyes in wastewater, *Sep. Purif. Technol.* 306 (2023) 122636.
[19] B. Xiang, J.L. Gong, Y.Q. Sun, J. Li, Robust PVA/GO@MOF membrane with fast photothermal self-cleaning property for oily wastewater purification, *J. Hazard. Mater.* 462 (2024) 132803.
[20] B. Hudaib, R. Abu-Zurayk, H. Waleed, A.A. Ibrahim, Fabrication of a novel (PVDF/MWCNT/polypyrrole) antifouling high flux ultrafiltration membrane for crude oil wastewater treatment, *Membranes* 12 (8) (2022) 751.
[21] W.G. Zheng, B. Shen, W.T. Zhai, Surface functionalization of graphene with polymers for enhanced properties, New Progress on Graphene Research, *InTech* (2013). http://dx.doi.org/10.5772/50490.
[22] A.T. Yasir, N. Ndame, N. Alshaibi, M. Dalloul, A.H. Hawari, A. Benamor, Enhancing the stability and performance of graphene oxide-poly(amido amine) polysulfone membranes with (3-aminopropyl)triethoxysilane crosslinker, *J. Environ. Chem. Eng.* 13 (2) (2025) 115989.
[23] A. Avornyo, C.V. Chrysikopoulos, Applications of graphene oxide (GO) in oily wastewater treatment: recent developments, challenges, and opportunities, *J. Environ. Manag.* 353 (2024) 120178.
[24] A.T. Yasir, A. Benamor, A.H. Hawari, Enhancement of polysulfone ultrafiltration membrane with third generation poly(amido amine)-graphene oxide nanocomposite, *J. Water Process Eng.* 54 (2023) 103991.
[25] N.F.D. Junaidi, N.H. Othman, N.S. Fuzil, M.S. Mat Shayuti, N.H. Alias, M.Z. Shahruddin, F. Marpani, W.J. Lau, A.F. Ismail, N.D. Aba, Recent development of graphene oxide-based membranes for oil–water separation: a review, *Sep. Purif. Technol.* 258 (2021) 118000.
[26] Z. Hosseinabadi-Farahani, H. Hosseini-Monfared, N.M. Mahmoodi, Graphene oxide nanosheet: preparation and dye removal from binary system colored wastewater, *Desalin. Water Treat.* 56 (9) (2015) 2382–2394.
[27] T.D. Kusworo, A.C. Kumoro, N. Aryanti, D.P. Utomo, H. Hasbullah, F.F. Lingga, A. Widiastuti, M. Yulfarida, F. Dalanta, T.A. Kurniawan, Photocatalytic antifouling nanohybrid polysulfone membrane using the synergetic effect of graphene oxide and SiO_2 for effective treatment of natural rubber-laden wastewater, *J. Membr. Sci.* 657 (2022) 120663.
[28] A. Kuzminova, M. Dmitrenko, A. Zolotarev, D. Markelov, A. Komolkin, R. Dubovenko, A. Selyutin, J. Wu, R.X. Su, A. Penkova, Novel mixed matrix membranes based on poly(vinylidene fluoride): development, characterization, modeling, *Polymers* 15 (5) (2023) 1222.
[29] Z. Hosseinabadi-Farahani, N.M. Mahmoodi, H. Hosseini-Monfared, Preparation of surface functionalized graphene oxide nanosheet and its multicomponent dye removal ability from wastewater, *Fibres. Polym* 16 (5) (2015) 1035–1047.
[30] S. Kamari, A. Shahbazi, High–performance nanofiltration membrane blended by Fe_3O_4@SiO_2–CS bionanocomposite for efficient simultaneous rejection of salts/heavy metals ions/dyes with high permeability, retention increase and fouling decline, *Chem. Eng. J.* 417 (2021) 127930.
[31] N.M. Mahmoodi, A. Maghsoodi, Kinetics and isotherm of cationic dye removal from multicomponent system using the synthesized silica nanoparticle, *Desalin. Water Treat.* 54 (2) (2015) 562–571.
[32] L.D. Feng, Y. Gao, Y. Xu, H.B. Dan, Y.F. Qi, S.Q. Wang, F.J. Yin, Q.Y. Yue, B.Y. Gao, A dual-functional layer modified GO@SiO_2 membrane with excellent antifouling performance for continuous separation of oil-in-water emulsion, *J. Hazard. Mater.* 420 (2021) 126681.
[33] H. Mahdavi, M.A. Kerachian, M. Abazari, Synergistic effect of GO@SiO_2 and GO@ZnO nano-hybrid particles with PVDF-g-PMMA copolymer in high-flux ultrafiltration membrane for oily wastewater treatment and antifouling properties, *J. Ind. Eng. Chem.* 108 (2022) 374–388.
[34] F. Ebrahimi, S.R. Nabavi, A. Omrani, Fabrication of hydrophilic special sandwich structure of PAN/GO/SiO_2 electrospun membrane decorated with SiO_2 nanoparticles for oil/water separation, *J. Water Process Eng.* 48 (2022) 102926.
[35] Y. Liu, J.Y. Liu, Y.H. Jiang, M.J. Meng, L. Ni, H.L. Qiu, R.G. Yang, Z.C. Liu, H.W. Liu, Synthesis of novel high flux thin-film nanocomposite nanofiltration membranes containing GO–SiO_2 *via* interfacial polymerization, *Ind. Eng. Chem. Res.* 58 (49) (2019) 22324–22333.
[36] L.N. Zhang, B.L. Chen, A. Ghaffar, X.Y. Zhu, Nanocomposite membrane with polyethylenimine-grafted graphene oxide as a novel additive to enhance pollutant filtration performance, *Environ. Sci. Technol.* 52 (10) (2018) 5920–5930.
[37] P.S. Parsamehr, M. Zahed, M.A. Tofighy, T. Mohammadi, M. Rezakazemi, Preparation of novel cross-linked graphene oxide membrane for desalination applications using (EDC and NHS)-activated graphene oxide and PEI, *Desalination (Amst.)* 468 (2019) 114079.
[38] C.N. Matindi, S. Kadanyo, G.S. Liu, M.Y. Hu, Y.X. Hu, Z.Y. Cui, X.H. Ma, F. Yan, B. Q. He, J.X. Li, Hydrophilic polyethyleneimine-TiO_2 hybrid layer on polyethersulfone/sulfonated polysulfone blend membrane with antifouling characteristics for the effective separation of oil-in-water emulsions, *J. Water Process Eng.* 49 (2022) 102982.
[39] L. Teng, C. Yue, G. Zhang, Epoxied SiO_2 nanoparticles and polyethyleneimine (PEI) coated polyvinylidene fluoride (PVDF) membrane for improved oil water separation, anti-fouling, dye and heavy metal ions removal capabilities, *J Colloid Interface Sci.* 630 (2023) 416–429.
[40] D.A. Hussein Al-Timimi, Q.F. Alsalhy, A.A. AbdulRazak, E. Drioli, Novel polyether sulfone/polyethylenimine grafted nano-silica nanocomposite membranes: interaction mechanism and ultrafiltration performance, *J. Membr. Sci.* 659 (2022) 120784.
[41] H. Chen, Q.H. Ye, X.L. Wang, J. Sheng, X. Yu, S.Y. Zhao, X.M. Zou, W.W. Zhang, G. Xue, Applying sludge hydrolysate as a carbon source for biological denitrification after composition optimization *via* red soil filtration, *Water Res.* 249 (2024) 120909.
[42] Y.C. Tang, Y.H. Wu, X. Tong, Y. Bai, W.L. Wang, Z. Chen, A. Xu, N. Ikuno, N. Koji, H.Y. Hu, Fouling characteristics and flux prediction model of reverse osmosis membrane based on hydrophobic fractions in reclaimed water, *Sep. Purif. Tech* 335 (2024) 126187.
[43] D.L. Chen, Q.Y. Wang, Y.B. Li, Y.D. Li, H. Zhou, Y.L. Fan, A general linear free energy relationship for predicting partition coefficients of neutral organic compounds, *Chemosphere* 247 (2020) 125869.
[44] J. Hermia, Blocking filtration. Application to Non-Newtonian Fluids, in: Mathematical Models and Design Methods in Solid-Liquid Separation, Springer, 2012.
[45] A.T. Yasir, A.H. Hawari, M. Talhami, M. Baune, J. Thöming, F. Du, The impact of electric field on the demulsification efficiency in an electro-coalescence process, *J. Electrost.* 122 (2023) 103796.
[46] A.T. Yasir, A. Benamor, A.H. Hawari, E. Mahmoudi, Graphene oxide/chitosan doped polysulfone membrane for the treatment of industrial wastewater, *Emerg. Mater* 6 (3) (2023) 899–910.
[47] W.S. Hummers Jr., R.E. Offeman, Preparation of graphitic oxide, *J. Am. Chem. Soc.* 80 (6) (1958) 1339.
[48] E. Mahmoudi, W.L. Ang, C.Y. Ng, L.Y. Ng, A.W. Mohammad, A. Benamor, Distinguishing characteristics and usability of graphene oxide based on different sources of graphite feedstock, *J. Colloid Interface Sci.* 542 (2019) 429–440.
[49] S.S. Dan, H. Bagheri, A. Shahidizadeh, H. Hashemipour, Performance of graphene oxide/SiO_2 nanocomposite-based: antibacterial activity, dye and heavy metal removal, *Arab. J. Chem.* 16 (2) (2023) 104450.
[50] D.Q. Wang, H.C. Ge, Preparation and characterization of polyethyleneimine functionalized magnetic graphene oxide as high uptake and fast removal for Hg (II), *Water Sci. Technol.* 86 (6) (2022) 1373–1387.
[51] R.E. Kesting, Phase inversion membranes, ACS Symposium Series (1985). https://doi.org/10.1021/bk-1985-0269.ch007.

[52] W. Zhang, W. Cheng, E. Ziemann, A. Be'er, X.L. Lu, M. Elimelech, R. Bernstein, Functionalization of ultrafiltration membrane with polyampholyte hydrogel and graphene oxide to achieve dual antifouling and antibacterial properties, *J. Membr. Sci.* 565 (2018) 293–302.
[53] C.Y. Liu, H.Y. Liu, C. Lu, K.Y. Tang, Y.Q. Zhang, Polyethyleneimine-modified graphene oxide/PNIPAm thermoresponsive hydrogels with rapid swelling/deswelling and improved mechanical properties, *J. Mater. Sci.* 52 (19) (2017) 11715–11724.
[54] N.Y. Ning, M.L. Wang, J. Zhang, L.Q. Zhang, M. Tian, Simultaneously improved actuated performance and mechanical strength of silicone elastomer by reduced graphene oxide encapsulated silicon dioxide, *Int. J Smart Nano Mater* 6 (4) (2015) 251–267.
[55] B. Ziółkowski, L. Florea, J. Theobald, F. Benito-Lopez, D. Diamond, Porous self-protonating spiropyran-based NIPAAm gels with improved reswelling kinetics, *J. Mater. Sci.* 51 (3) (2016) 1392–1399.
[56] R. Dong, L.M. Wang, J.C. Zhu, L.L. Liu, Y.L. Qian, A novel SiO_2–GO/acrylic resin nanocomposite: fabrication, characterization and properties, *Appl. Phys. A* 125 (8) (2019) 551.
[57] C. Xing, C.Y. Liu, C. Lai, S.Q. Zhang, Tuning d-spacing of graphene oxide nanofiltration membrane for effective dye/salt separation, *Rare Met.* 42 (2) (2023) 418–429.
[58] L. Yan, Q. Zhao, T. Jiang, X. Liu, Y. Li, W. Fang, H. Yin, Adsorption characteristics and behavior of a graphene oxide-Al13 composite for cadmium ion removal from aqueous solutions, *RSC Adv.* 5 (83) (2015) 67372–67379.
[59] K. Li, Q.F. Liu, H.F. Cheng, M.S. Hu, S. Zhang, Classification and carbon structural transformation from anthracite to natural coaly graphite by XRD, Raman spectroscopy, and HRTEM, *Spectrochim. Acta Mol. Biomol. Spectrosc.* 249 (2021) 119286.
[60] A. Kocyigit, İ. Karteri, I. Orak, S. Uruş, M. Çaylar, The structural and electrical characterization of Al/GO-SiO_2/p-Si photodiode, *Phys. E Low Dimension. Syst. Nanostruct.* 103 (2018) 452–458.
[61] A.F. Ghanem, A.M. Youssef, M.H. Abdel Rehim, Hydrophobically modified graphene oxide as a barrier and antibacterial agent for polystyrene packaging, *J. Mater. Sci.* 55 (11) (2020) 4685–4700.
[62] G. Surekha, K. Venkata Krishnaiah, N. Ravi, R. Padma Suvarna, FTIR, Raman and XRD analysis of graphene oxide films prepared by modified Hummers method, *J. Phys. Conf. Ser.* 1495 (1) (2020) 012012.
[63] G.S. Wu, L.C. Ma, L. Liu, L. Chen, Y.D. Huang, Preparation of SiO_2–GO hybrid nanoparticles and the thermal properties of methylphenylsilicone resins/SiO_2–GO nanocomposites, *Thermochim. Acta* 613 (2015) 77–86.
[64] Y.C. Du, L.J. Huang, Y.X. Wang, K. Yang, Z.J. Zhang, Y. Wang, M.J. Kipper, L.A. Belfiore, J.G. Tang, Preparation of graphene oxide/silica hybrid composite membranes and performance studies in water treatment, *J. Mater. Sci.* 55 (25) (2020) 11188–11202.
[65] X.M. Tan, D. Rodrigue, A review on porous polymeric membrane preparation. Part I: production techniques with polysulfone and poly (vinylidene fluoride), *Polymers* 11 (7) (2019) 1160.
[66] A.T. Yasir, N. Alshaibi, N. Ndame, H. Ben Youssef, M.M. Ba-Abbad, A. Benamor, Synthesis of novel graphene oxide-chitosan-silicon dioxide nanocomposite embedded in polysulfone membrane for oily water treatment, *Water Conserv. Sci. Eng.* 9 (2) (2024) 79.
[67] Y. Elhamarnah, H. Qiblawey, M. Nasser, Synergistic effects of deep eutectic solvents on the morphology and performance of polysulfone ultrafiltration membranes, *J. Environ. Manag.* 370 (2024) 122920.
[68] A. Alkhouzaam, H. Qiblawey, Synergetic effects of dodecylamine-functionalized graphene oxide nanoparticles on antifouling and antibacterial properties of polysulfone ultrafiltration membranes, *J. Water Process Eng.* 42 (2021) 102120.
[69] M.K. Khan, Q.Y. Wang, M.E. Fitzpatrick, Atomic force microscopy (AFM) for materials characterization, in: Materials Characterization Using Nondestructive Evaluation (NDE) Methods, Elsevier, 2016, p. 16.
[70] Y. Li, G.Y. Pan, Y. Zhang, J. Wang, H. Yu, G.K. Zhao, M.H. Zhao, G.Q. Tang, Y. Guo, C.J. Wu, Y.Q. Liu, A new method for tailoring the surface pore size and internal pore structure of ultrafiltration membranes without using additives: atomization-assisted nonsolvent induced phase separation method, *Sep. Purif. Technol.* 304 (2023) 122334.
[71] T.P.N. Nguyen, R. Dufour, V. Thomy, V. Senez, R. Boukherroub, Y. Coffinier, Fabrication of superhydrophobic and highly oleophobic silicon-based surfaces *via* electroless etching method, *Appl. Surf. Sci.* 295 (2014) 38–43.
[72] K.J. Hwang, C.Y. Liao, K.L. Tung, Effect of membrane pore size on the particle fouling in membrane filtration, *Desalination (Amst.)* 234 (1–3) (2008) 16–23.
[73] S.L. Tan, S. El Meragawi, M. Majumder, E. Von Lau, Superhydrophilic and underwater superoleophobic graphene oxide-phytic acid membranes for efficient separation of oil-in-water emulsions, *Sep. Purif. Technol.* 314 (2023) 123544.
[74] J.H. Gu, Z. Qu, X.N. Zhang, H.W. Fan, C.X. Li, J. Caro, H. Meng, Membrane contact demulsification: a superhydrophobic ZIF-8@rGO membrane for water-in-oil emulsion separation, *Engineering* 23 (2023) 73–81.
[75] X.H. Xiao, Z.X. Yu, X.M. Zhu, J. Wang, Q.C. Xiang, Sepiolite@TiO_2/Graphene oxide composite membrane for long-term separation of oily wastewater, *J. Mol. Struct.* 1273 (2023) 134258.
[76] Z.C. Li, W. Xie, Z. Zhang, S.X. Wei, J.Q. Chen, Z.L. Li, Multifunctional sodium alginate/chitosan-modified graphene oxide reinforced membrane for simultaneous removal of nanoplastics, emulsified oil, and dyes in water, *Int. J. Biol. Macromol.* 245 (2023) 125524.